



Study of the Laser Metal Deposition (LMD) technology in the automotive industry

Master degree in Automotive Engineering

Francisco Miguel Quaresma Ramalho

Leiria, September of 2019



Study of the Laser Metal Deposition (LMD) technology, in the automotive industry

Master degree in Automotive Engineering

Francisco Miguel Quaresma Ramalho

Project under the supervision of Professor Maria Leopoldina Alves, and Professor Mário Simões Correia

Leiria, September of 2019

Originality and Copyright

This project report is original, made only for this purpose, and all authors whose studies and publications were used to complete it are duly acknowledged.

Partial reproduction of this document is authorized, provided that the author is explicitly mentioned, as well as the study cycle, i.e., Master degree in Automotive Engineering, 2018/2019 academic year, of the School of Technology and Management of the Polytechnic Institute of Leiria, and the date of the public presentation of this work.

Dedication

I am dedicating this thesis to my mother and father, who have always loved me, believed in me, and provided me with the necessary conditions so I could go as far as I wished in life.

I would also like to dedicate this thesis to my maternal grandparents, who sadly are no longer among us, but who always supported and loved me for as long as they were with me.

All of their words of motivation and care push me towards my goals every day, and will continue doing so.

Acknowledgments

During the execution of this project, I have received a large amount of assistance and guidance, which helped me go through every obstacle that arose during this period.

Firstly, I would like to thank IK4-Tekniker, whom has made themselves available, to hear the guidelines of the project, before it had even started, and readily made several LMD produced components available to me, so I could conduct the study that was designed.

Additionally, I would like to thank Trumpf, whom has also made themselves available for a talk in which it was possible to obtain valuable information about the technology that was studied in this project.

I would also like to thank, Dr. Amilcar Ramalho, and Dr. Luis Vilhena, as well as the ICEMS of the University of Coimbra, which provided their expertise as well as their equipment on the execution of the friction and wear tests, as well as the impulse excitation of vibration test.

Adding to both the companies that helped, I would like to thank my supervisor, Dr. Maria Leopoldina Alves, with whom this project started, as a smaller study, ending up evolving into the present project. Her expertise and guidance were invaluable, for both the theoretical research as well as for the methodology.

I would also like to thank, my second supervisor, Dr. Mário Correia, who despite only joining the project in later date, also ended up providing me with his expertise and guidance, for the theoretical research and also for the methodology.

I would also like to thank Eng. Fernanda Carvalho, who as provided me with guidance on the experimental part of the project, assisting and providing her expertise on the matter.

Abstract

The last few decades in the automotive industry have been marked by a heavy concern with the environment, saving energy and reducing material wastage, while aiming to maintain good mechanical properties, essential in the components usage.

Additive manufacturing (AM) techniques present themselves as a viable option in the matter, with Laser Metal Deposition (LMD), rising as one of the most promising techniques within this category, capable of producing near-net shape components, with a layer upon layer construction of three-dimensional solid parts from a 3D CAD model, with good mechanical properties and acceptable surface finishing.

Laser Metal Deposition is a relatively recent technique, which is made noticeable by the lack of clarification about the influence of several parameters in the final component's characteristics, ultimately leading to a scarce availability of the process in the market.

This paper aims to clarify and evaluate, how LMD produced parts can suit the automotive industry, by measuring and analysing their behaviour under several mechanical tests.

Keywords: Laser Metal Deposition, Additive Manufacturing, Automotive Industry.

Contents

Originality and Copyright	iii
Dedication.....	iv
Acknowledgments.....	v
Abstract	vi
List of Figures	ix
List of Tables.....	xii
List of Abbreviations and Acronyms.....	xiv
1. Introduction	1
1.1. Objectives	2
1.2. Structure of the project.....	2
2. Theoretical framework.....	4
2.1. Metal additive manufacturing processes.....	4
2.2. Laser metal deposition	8
2.2.1. Powder and wire LMD	12
2.2.2. Metallic wire.....	14
2.2.3. Metallic powder.....	15
2.2.4. Laser technology.....	16
3. Materials and methodology	19
3.1. Experimental LMD components	19
3.2. Component preparation.....	25
3.3. Methodology.....	27
3.3.1. Surface preparation.....	29
3.3.2. Microhardness test.....	30
3.3.3. Density test	33
3.3.4. Optical microscopy test	34
3.3.5. Impulse excitation of vibration test	37
3.3.6. Friction and Wear test.....	38
4. Results and discussion	41
4.1. Microhardness test	41

4.2. Density test.....	44
4.3. Optical microscopy test.....	46
4.4. Impulse excitation of vibration test	48
4.5. Friction and Wear test	51
5. Conclusion.....	63
6. Future work	66
Bibliography	67

List of Figures

Figure 1 - Manufacturing cost variation per manufactured number of parts ^[10]	7
Figure 2 - Illustration of an LMD deposition process ^[18]	10
Figure 3 - Graphical representation of the molten pool area ^[17]	10
Figure 4 - Schematic representation of layer deposition in LMD technology ^[16]	10
Figure 5 - LMD deposition process, with robotic control, application ^[20]	12
Figure 6 - Schematic representation of wire drawing ^[27]	14
Figure 7 - Schematic representation of the first designed ruby laser ^[36]	17
Figure 8 - Components produced by IK4-Tekniker and provided for analysis ^[37]	19
Figure 9 - SEM photomicrographs of Metco 42C metallic powder ^[40]	20
Figure 10 - Component P1 (left) and P2 (right) originally provided by IK4-Tekniker.....	22
Figure 11 - Component P3 (left) and P4 (right) originally provided by IK4-Tekniker.....	22
Figure 12 - Component P5 originally provided by IK4-Tekniker.....	23
Figure 13 - Deposition strategy for the base, which is repeated on the z-axis, overlaying layers, creating the final powder components ^[39]	23
Figure 14 - Component W1 (left) and W2 (right) originally provided by IK4-Tekniker.....	24
Figure 15 - Component W3 (left) and W4 (right) originally provided by IK4-Tekniker.....	24
Figure 16 - Component W5 originally provided by IK4-Tekniker.....	24
Figure 17 - Deposition strategy for the base, which is repeated on the z-axis, overlaying layers, creating the final wire components ^[39]	25
Figure 18 - The equipment Struers Labotom-3 used to separate the deposited material from the substrate. ...	26
Figure 19 - Representation of a wire (left) and powder (right) component after the separation between the substrate and the deposited material.....	26
Figure 20 - Graphic representation of the conducted mechanical tests, in a timeline.....	28
Figure 21 - Surface polishing preparation process.....	29
Figure 22 - The Struers RotoPol-21 equipment, the polishing machine used to prepare the components for microhardness testing.....	30
Figure 23 - Representation of a bad surface finish, with too many scratching, due to bad polishing.....	31
Figure 24 - Vickers hardness test ^[44]	32
Figure 25 - Comparison between the ideal indentation (left picture) and a real indentation (right picture)....	32

Figure 26 - Representation of the area subjected to the microhardness Vickers test.	33
Figure 27 - Density testing apparatus.....	34
Figure 28 - Detail of the cut components for density testing.	34
Figure 29 - Detail of the small pieces cut from components W2 (on the left) and P2 (on the right) for the optical microscopy test.....	35
Figure 30 - Detail of the specimen mirrored surface finish.....	36
Figure 31 - Mechanical vibration test apparatus ^[48]	38
Figure 32 - Wear testing apparatus ^[51]	39
Figure 33 - Microhardness test results for components P1 (left) and P2 (right).	41
Figure 34 - Microhardness test results for components P3 (left) and P4 (right).	41
Figure 35 - Microhardness test results for components P5 (left) and W2 (right).....	41
Figure 36 - Graphical representation of the relation between the deposition height and the microhardness tendency line slope (left) and standard deviation (right).....	43
Figure 37 - Identifiable gaps on component W2, after performing a vertical cut.	45
Figure 38 - Identifiable gaps on component W2, after performing a horizontal cut.	46
Figure 39 - Single layer disposition (left) and horizontal layer overlap (right) on component P2.....	46
Figure 40 - Layer disposition, with evidence of possible gap formation on component P2.....	47
Figure 41 - Layer disposition on component W2.....	47
Figure 42 - Component P2 (left) and W2 (right) microstructure.	48
Figure 43 - Experimental and analytical response to the impulse excitation of component W2.....	49
Figure 44 - Vibration spectra of component W2.....	49
Figure 45 - Vibration spectra of component P2.	50
Figure 46 - Component W2 base friction coefficient variation during reciprocating sliding tests.....	51
Figure 47 - Component W2 top friction coefficient variation during reciprocating sliding tests.....	52
Figure 48 - Component P2 base friction coefficient variation during reciprocating sliding tests.	53
Figure 49 - Component P2 top friction coefficient variation during reciprocating sliding tests.	53
Figure 50 - Cross section profiles from the wear tracks on the base part (left) and top part (right) of the W2 component, for 3, 5 and 7 N of normal force.	57
Figure 51 - Cross section profiles from the wear tracks on the base part (left) and top part (right) of the P2 component, for 3, 5 and 7 N of normal force.	57
Figure 52 - Quadratic curves used to represent the wear profiles cross sections.	58

Figure 53 - Comparison between the base and top wear rate coefficients, for component W2 (left) and component P2 (right)..... 60

Figure 54 - Comparison between the base and top cross section area of the wear profile, on W2 (left) and P2 (right) specimens. 60

List of Tables

Table 1 - Comparison between AM and conventional manufacturing techniques, in industry applications ^[10] .	7
Table 2 - DIN C45E typical main mechanical properties ^[38] .	20
Table 3 - Metco 42C (equivalent to AISI 431 Stainless Steel) typical mechanical properties ^[34] .	21
Table 4 - AISI 316L Stainless Steel typical mechanical properties ^[41] .	21
Table 5 - Powder LMD components dimensions (x, y, z).	23
Table 6 - Wire LMD components dimensions (x, y, z).	25
Table 7 - Chemical composition of the used etchants for component W2 (left) ^[46] and P2 (right) ^[47] .	36
Table 8 - Zirconium sphere mechanical properties ^[50] .	39
Table 9 - Microhardness test results.	42
Table 10 - Density test results.	45
Table 11 - Mechanical elastic properties, obtained through impulse excitation of vibration testing, for components W2 and P2.	50
Table 12 - Relation between density for components W2 and P2.	50
Table 13 - Wear scars left on the zirconium sphere for component W2.	54
Table 14 - Wear scars left on the zirconium sphere for component P2.	55
Table 15 - Zirconium sphere wear scars diameters, depth (h) and volume (V) of the wear scars, and wear rate (k) of the component W2.	55
Table 16 - Zirconium sphere wear scars diameters, depth (h) and volume (V) of the wear scars, and wear rate (k) of the component P2.	56
Table 17 - Point coordinates of the quadratic curves used to represent the wear profile cross section on the W2 specimen base part.	58
Table 18 - Point coordinates of the quadratic curves used to represent the wear profile cross section on the W2 specimen top part.	58
Table 19 - Point coordinates of the quadratic curves used to represent the wear profile cross section on the P2 specimen base part.	59
Table 20 - Point coordinates of the quadratic curves used to represent the wear profile cross section on the P2 specimen top part.	59
Table 21 - Wear profile cross section approximate area of specimen W2 base and top parts.	59
Table 22 - Wear profile cross section approximate area of specimen P2 base and top parts.	59
Table 23 - Wear rate coefficient on the plane side, for both the W2 and P2 components.	60

List of Abbreviations and Acronyms

AM	Additive Manufacturing
ASTM	American Society for Testing and Materials
CNC	Computer Numerical Control
DLF	Directed Light Fabrication
EBFFF	Electron Beam Free Form Fabrication
ESTG	School of Technology and Management
LASER	Light Amplification by the Stimulated Emission of Radiation
LENS	Laser Engineered Net Shaping
LMD	Laser Metal Deposition
SEM	Scanning Electron Microscope
STL	Stereo Lithography

1. Introduction

European Union regulations are in constant evolution, demanding that car manufacturers have increasingly lower pollutant emissions every year, which ultimately leads manufacturers to invest large amounts of money in research and development, to come up with more efficient and environment-friendly ways of manufacturing their vehicles.

The technical capabilities that brands acquire with this R&D allow them not only to accomplish the restrict regulations, but also to gain a competitive advantage over the contestants in the automotive industry.

The focus of a car-producing brand, in everyday life, is to achieve acceptable quality in its vehicles, conjugating that with a maximum reduction of costs and emissions of pollutants, allowing to accomplish the impositions and still maintain a competitive position in the market.

In this context, additive manufacturing (AM) technologies present themselves as a viable alternative to those which are considered the more conventional manufacturing processes, since they allow waste reduction of raw materials and significant energy savings, as well as a reduction in production time, points that constitute a strong basis, strong enough for further developments to be carried out on this type of technology.

Within these additive manufacturing processes, the LMD (Laser Metal Deposition) technology presents itself as a strong alternative to replace processes of a subtractive nature, once it allows the production of near-net shape metallic components, with good mechanical properties that can satisfy most of the purposes to which they are intended.

The LMD technology presents advantages at an energetic level, reveals low material waste, lower production times when comparing with conventional manufacturing processes and a good reproducibility, factors that make it a strong candidate to take on a role in the automotive industry of the future.

Despite the mentioned advantages of the LMD technology, the majority of automotive brands still have some uncertainty about its applicability to their production lines, due to the fact of it being a relatively recent technology, meaning that the feasibility of its application is still something being studied.

Currently the main applications of LMD technologies are essentially related to coating and repairing processes of new or already existent parts, which allow to obtain surfaces with high hardness and mechanical resistance, meaning that the production of near-net shape components is yet to be applied to production lines, much because of the youthfulness of the process.

The influence that various parameters have in the process, such as power, width and distance to the deposition substrate of the laser beam, and the flow and distance to the deposition substrate of the feed of metallic material, is not yet well defined, with scarce documentation available, highlighting the pertinence of carrying out a study on this topic.

It should be noticed that, as mentioned, the youthfulness of the technology along with its complexity, means that the production of components is still costly. Adding to this, there is also a lack of standardized equipment and material on the market, preventing the process to be applied on a larger scale.

Having the above mentioned in mind, a study to characterize the influence of each parameter on the final product would imply a high number of tests, making it economically demanding, especially taking into account that this study must be performed in a restricted time window.

Therefore, combining a more viable economical context to a more restricted time frame, a suitable project can be in fact idealized, starting from the principle that there is a set of optimized parameters that allow the production of model components, allowing to use these to evaluate what are the main mechanical characteristics of these components, which allows to obtain a widespread characterization of what can be expected when using LMD technologies.

1.1.Objectives

This project sets as its main goal, to study the mechanical properties of several LMD components produced with both powder and wire LMD processes, using several deposition heights on the powder LMD components, starting with the available information on the bibliography, and finishing in a place where new information can be achieved in order to either complement or increment the already existent information.

In order to achieve the main goal, it is necessary to firstly, understand how both powder and wire LMD components compare within themselves, in a mechanical behaviour point of view, also analysing how the deposition height affects this comparison.

Secondly, it is necessary to understand, how the mentioned LMD components, compare to components produced with conventional manufacturing techniques, also on a mechanical behaviour point of view.

With the information gathered, while trying to achieve the main goals, a less critical goal, was to try and understand, if LMD produced components are in fact feasible for use on the automotive industry.

1.2.Structure of the project

The project was designed to be presented in this report in several chapters, which represent the order in which the work was developed.

The introductory chapter, is where both the theme and the major goals are presented, creating a clear panorama of what was set to achieve by the end of this project.

The second chapter, “Theoretical framework”, is where the state of the art is analysed, helping to understand how the technology under analysis was born, in what state it is in the present, and where can it go in the future.

The third chapter, “Materials and methodology”, is where a presentation is made of exactly what were the available materials to conduct the study, and also, how the study was scheduled regarding the mechanical tests and the preparation for them.

The fourth chapter, “Results and discussion”, is where all of the results that were obtained from the mechanical tests were analysed, in order to understand exactly what information can be achieved with this project.

The fifth and final chapter, “Conclusions”, is where all of the information is filtered, presenting only the core conclusions that were taken from the mechanical tests.

2. Theoretical framework

Laser Metal Deposition is one of the metal additive manufacturing processes currently existent. To better understand how LMD technology was developed, a brief analysis upon the broad category of additive manufacturing (AM), as well as its relationship with metallic materials is important to be performed.

As so, to offer a more detailed overview of the technology under investigation, a few aspects of its basis are shown in this chapter, with a brief look into the history of AM processes, some economic aspects connected with them, their advantages as well as the limitations, the use of metallic materials and finally the main forms that exist nowadays.

2.1. Metal additive manufacturing processes

ASTM International, defines additive manufacturing, as “a process of joining materials to make objects from 3D model data, usually layer upon layer, as opposed to subtractive manufacturing methodologies.”^[1], with this definition being applicable not only to metals, but also to ceramics, polymers, composites and biological systems.

The first attempt to deposit a material in a manual layered build-up dates from 1934, when Anton^[2] used combustion reactions, in the form of oxy-fuel welding, to melt a type of metal, indicating that the early days of AM actually started with metallic materials. However, there were serious accuracy and resolution issues due to the primitiveness of the technology, leading to attempts of enhancing the process used to melt the metal. Even though, these were classified as a primitive form of additive manufacturing, one cannot fully classify them as so.

Despite the fact that AM processes started to be designed using metallic materials, it was not with these that the first big steps of development were made, given that the equipment necessary to achieve the melting of the metallic materials was not available, at least in an efficient level.

Modern additive manufacturing processes were presented by Munz^[3] that used stereolithography models in 1951. Later, in 1968, Swaison^[4] had the idea of using a laser beam to solidify photosensitive polymers. It was only in 1971 that Ciraud^[5], presented research that addressed the use of powder, partially melted by a laser, electron or plasma beam. All this research led to 1981, the year when Housholder^[6] first presented “Powder Laser Sintering” and Kodama^[7] published research about the first rapid prototyping system, with these two being the first true additive manufacturing systems.

However, it was only in 1986 that AM technologies started to be commercialized, with several companies joining the market^[8].

At the same time that AM technology entered the market, a more exhaustive research regarding the use of metal within this type of process started to be conducted.

One of the first documented studies that attempted to use metal as a deposit material in AM processes dates from 1986, in the University of Texas, in Austin ^[9]. Researchers that were carrying out studies using polymer in the form of powder, to create parts, layer by layer, with the main goal of manufacturing a full component, decided to study how metal would behave under the same conditions. This is believed to be one of the first attempts of metal additive manufacturing in history, in a modern form.

Since then the major part of research is focusing on making the technology more suitable for commercial and industrial use, with efforts being made to improve the properties of the components being produced.

Taking a closer look at the fundamentals for metal additive processes it is possible to understand that there are several aspects that need further improvements and studies.

One of the main aspects that is being faced relates to the highly variable thermal cycles that the deposited layers go through, which highly influence the properties of AM produced parts. All in all, this ends up being considered a limitation due to the fact that, to this day, it is relatively unknown how this thermal variance influences the components in a broad variety of materials, because most of the research was conducted with TC4 titanium alloy, with most of the other metallic materials being still under study ^[10].

Another relevant aspect is related to the reproducibility of parts and properties, since machine-to-machine variance is still relatively high, showing a need to create a more solid way to control these aspects and standardizing it.

However, and taking a broader look into the AM panorama, the scenario is highly positive, with the creation of a committee in 2009 by ASTM specifically for AM technologies, strengthening the importance of this family of manufacturing processes. The mentioned committee, the F42 Committee, has released several standards regarding the technology and the various aspects related to it ^[10].

All these achievements over history led to a family of technologies capable of competing face to face with the more conventional methods of manufacturing.

AM systems can be taken down and separated into categories, by dividing them by material feed stock, energy source and build volume, amongst other aspects.

There are many types of AM technologies, however, the more relevant ones for this project are, powder bed systems, powder feed systems and lastly wire feed systems ^[10].

The first type, by no specific order, is the powder bed system. There are two main parts of this system, a powder bed and an energy source. The powder bed is constituted out of the material in which the component will be made and the energy source is usually either a laser or an electron beam. The movement of the energy source over the powder bed, or vice versa,

allows the melting or sintering of the powder into the desired shape. Repeating this action layer by layer will end up in the manufacturing of the full component.

The second type of AM process is the powder feed system. This system is composed by a deposition head in which the powder is fed and melted, allowing its deposition into a surface on which the part is manufactured layer by layer.

The last type of AM processes is the wire feed system. This type of system is similar to the powder feed system, with the main difference being that the deposition material is in the form of a wire. Much like powder feed systems, there is an extruder head into which the wire is fed and then melted allowing its deposition.

Metallic materials are currently use for each of the three types of AM technologies, with some being more suitable to one type then others. However, on the list of most commonly used metals in AM technologies it is possible to find titanium alloys, such as TC4 and titanium aluminides, aluminium alloys, nickel alloys, tool steels, super alloys such as Inconel, and stainless steels such as AISI 316, 316L, 420 and 347.

In terms of economy, the growth that has been registered upon the application of AM processes on the broad variety of industries is truly remarkable.

In 2011, AM technologies had sales of roughly 1.6 billion euros. Previsions made in 2014 ^[10], estimated that by 2020 AM technologies could reach 6.5 billion euros in sales, but now, looking at 2018 reports, it is possible to note that AM technologies have reached sales of approximately 8.1 billion euros, which means that expectations were widely surpassed ^[11].

In 2014, Frazier stated that if all barriers that AM technologies faced were addressed, sales of up to 87 billion euros per year could be achievable. These barriers were identified to be related to the deposition rate, the material costs and the capability of monitoring the process to reduce process variance. It is also very important to train designers for AM projects, to create standards for the industry and to optimize AM materials ^[10].

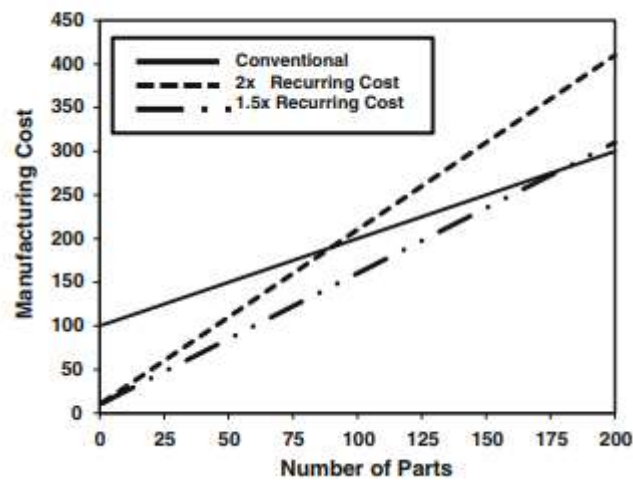
Several other studies have been conducted, with the goal of evaluating the economical saves that AM technologies could offer to working companies. Gnam ^[12] studied an application where Inconel 625 turbine blades were repaired by LENS technology and got to the conclusion that saves could reach the 1.2 million euros per year mark. Kelly ^[13] estimated savings of up to 81% when applying LENS technology to repair engine blade tips. Phinazwee ^[14] stated 79% greater material utilization and 56% cost savings when using Sciaky EBFFF technology to manufacture a typical airframe component of TC4 Titanium Alloy. Kinsella ^[15] registered a 30% cost saving when using electron beam wire deposition, as opposed to conventional methods, to deposit features on a forged engine case.

All these studies allowed Frazier ^[10] to reach several conclusions about the economic advantages and limitations of AM technologies. Table 1 resumes the comparison between AM and conventional manufacturing techniques, in industry applications.

Table 1 - Comparison between AM and conventional manufacturing techniques, in industry applications ^[10].

AM processes	Conventional techniques
Low production volumes and prototyping	Large production volumes
High material and machining cost	Low material cost
Capital investment	Easily processed or machined materials
Lower logistic and transportation cost	Centralized manufacturing

Frazier went on to build a model on which he showed the relation between the manufacturing cost *versus* the number of parts produced. The model created is presented below (fig. 1).

**Figure 1 - Manufacturing cost variation per manufactured number of parts ^[10].**

Looking at the graph in figure 1, the point in which each line crosses the y-axis, represents the fixed cost of each alternative, which is related to the cost of tools and manufacturing floor space, as for the slope, it represents the recurring cost of each alternative, which is related to the cost of raw material. Analysing each cost, it is possible to understand that AM alternatives represent lower costs on what tools and manufacturing floor space is related, however, the raw material is usually much more expensive, making it more suitable for small number of parts productions.

Although the speed, versatility and adaptability of AM technologies can also be highly valuable, these were not included as variables in the model shown before (Fig. 1), mostly because of the difficulty of quantifying those advantages.

2.2. Laser metal deposition

Now that the broad category of AM processes has been introduced, in chapter 2.1, it is important to introduce Laser Metal Deposition technology (LMD).

The youthfulness of LMD technology translates into several aspects, one of which is the fact that several different designations are used for the same technique. Amongst these it is possible to find “Laser Cladding”, “Directed Light Fabrication”, “Laser Engineered Net Shaping”, “Laser Direct Metal Deposition”, among others.

However, despite the different designations, the core of the technology is often similar, an additive manufacturing technique, with a layer upon layer construction of three-dimensional solid parts, using a feed of metallic material in the form of powder or wire, and a high-power laser source to melt the fed material.

The material is fed through a nozzle onto a surface (substrate) where it forms a linear layer, which side by side then creates a full layer. The vertical overlap of these layers then results in the desired 3D component.

Laser metal deposition is as of today one of the most promising laser assisted metal AM processes in development, since it offers the possibility to build near net shape components with complex geometries, while maintaining the possibility of rapid prototyping, design freedom, low production times, low dilution rates (although it varies significantly from wire to powder raw material) and good surface properties.

Another strong point in favour of LMD is that it is capable of carrying out coating and repairing processes in already existent components, offering excellent mechanical resistance to the surface onto which it is applied.

The history behind the technologies that over time developed into LMD, was shortly presented previously, however, there were a few points in time that are heavily related to the development of the LMD technology that haven't been discussed yet.

First and foremost, it is important to remember that one of the barriers that made AM technologies stick with polymers was connected to the fact that the laser technology available at that time had not enough power, making them incapable of working with metallic materials. However, researchers first tackled a few other issues, working only with polymers, before metallic materials were contemplated ^[16].

In the beginnings of AM development, one of the biggest challenges was related to the fact that the components being produced were lacking in accuracy and resolution, preventing the use of those components for an industrial purpose. This meant that near-net shape manufacturing was almost impossible, since there was a lack of control over the material deposition.

It was only in the 1980's, that researchers started to develop both laser and microprocessor technology that were capable of managing the deposition, offering both accuracy and

resolution. However, this technology was still not enough to contemplate the use of metallic materials, since higher laser power and better control was still necessary.

It was around the 1990's, when the connection between CAD CAM technologies and laser assisted AM processes was made, offering the possibility to develop models with the assistance of a computer, that interest started to rise. This changed the strategy of deposition completely, with the use of planar slicing and meshing techniques to create stereo-lithographical files, making the entire process much easier to control.

Despite all these developments, the main use was still linked with polymers, used to produce models that verified form and fit.

It was still in the early 1990's that metallic materials started to be tested, manufacturing patterns used in investment casting. This made clear that laser assisted AM techniques could offer both fast and economical rapid prototyping capabilities ^[16].

The process as we know it now, was first developed in two locations, first at Los Alamos National Laboratory and secondly at Sandia National Laboratory.

Given that a major part of the aspects connected to the process were being developed almost from the ground, each team gave it different designations, with Los Alamos National Laboratory developing what they called Directed Light Fabrication (DLF), and Sandia National Laboratory developing Laser Engineered Net Shaping (LENS). The main core of the processes was however, identical, with a continuous supply of metal powder being fed directly to the laser focal zone, where it was melted and re-solidified in the wake of a molten pool, with the feeder and laser head stock moving across the area where the part is being produced.

Both forms of what is now called LMD developed throughout time, ending up with a few changes from the initial process.

In summary, much like it was already mentioned, LMD in its current shape, is an AM technique, with a layer upon layer construction of three-dimensional solid parts, where metal in the form of powder or wire is used as raw material, is introduced to the processing zone and melted using a high-power laser beam.

A schematic representation of the process is shown in figure 2. In the picture it possible to visualize that the laser beam involves the powder that is being fed into the substrate, melting it into a liquid form, to deposit it in the molten pool, where it will later solidify creating a solid layer.

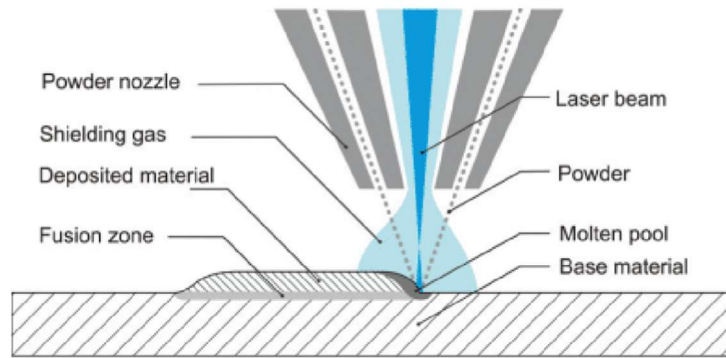


Figure 2 - Illustration of an LMD deposition process [18].

The metal is directly deposited in the already referenced molten pool, where the material is in liquid form, surrounded by solid metal, which allows the layer to be held in its place through surface tension, making overhead depositions possible. The control of this molten pool, presented in figure 3, is what ultimately determines the characteristics of the deposited material, with the cooling rate and solidification velocity being the main influencers of the size, orientation and composition of the microstructure, affecting the deposit strength and ductility.

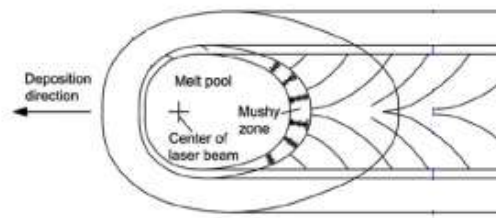


Figure 3 - Graphical representation of the molten pool area [17].

Figure 4, presents a schematic of the deposition of several layers, offering a clear idea of how components are produced by LMD.

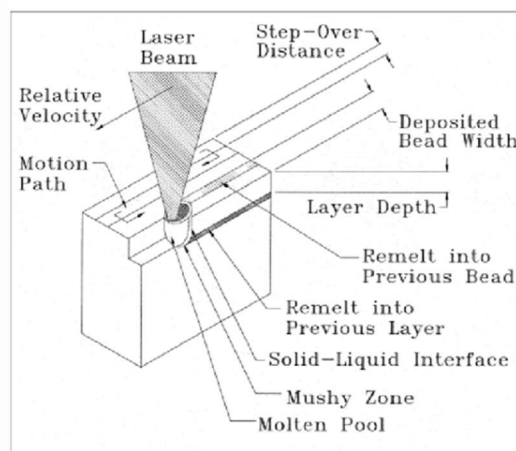


Figure 4 - Schematic representation of layer deposition in LMD technology [16].

The deposition of successive layers means that the cooling rate through the piece is highly variable, especially if the deposition is continuous, meaning that the layers on the bottom will cool much slower than the layers on the top of the part, assuming a vertical deposition strategy.

Another factor to take in consideration is the horizontal and vertical overlap used, since these will affect the layer dimensions, in its width and thickness.

Usually, excessive horizontal (lateral) overlap may result in defective material usage efficiency, on the other hand, too low of a horizontal overlap can result in high surface roughness, which can compromise the deposition of multiple layers, since discontinuities are magnified by the number of layers deposited ^[19].

Regarding the vertical overlap, it is highly dependent on the height homogeneity of each layer upon where the deposition is made ^[19] and an excessively large or small value can affect the surface hardness since the already deposited layers are excessively re-melted, influencing the cooling process.

The mechanical properties that components manufactured with LMD present are usually comparable to the ones typical in components manufactured recurring to the more conventional techniques, with experiments made using DLF process, another designation to LMD, showing that the yield strength obtained is higher than the one obtained with conventional processes when using 316 Stainless Steel and Inconel 690. Tensile properties of DLF components can be identical to the ones obtained in wrought material, which indicates that extra thermo-mechanical treatments, such as chemical and thermal homogenization, may not be needed ^[16].

As for the path of the powder/wire feeder and the laser head, it can be determined and controlled using different techniques. Both DLF and LENS technologies used different strategies, with the DLF technology using a CNC (Computer Numerical Control) tool path and the LENS technology using a STL (stereo lithography) format. Both strategies complement the use of up to 5-axis of movement, with the possibility of adding more axis and robotic control resulting in additional degrees of freedom ^[16].

Robotic control is part of one of the many LMD capabilities, since it allows the possibility of depositing in different orientations not having to stick with vertical, top to bottom deposition. The deposition can also be made through the movement of the substrate while keeping both the laser and the feed stock stationary, or even using movement in all the components of the system (the laser and the feed stock combination and the substrate), since there is no need to use support layers, which can be useful in some situations ^[16].

Figure 5 shows an example where the laser and the feed stock are stationary, and the substrate moves through robotic control, offering high design freedom.

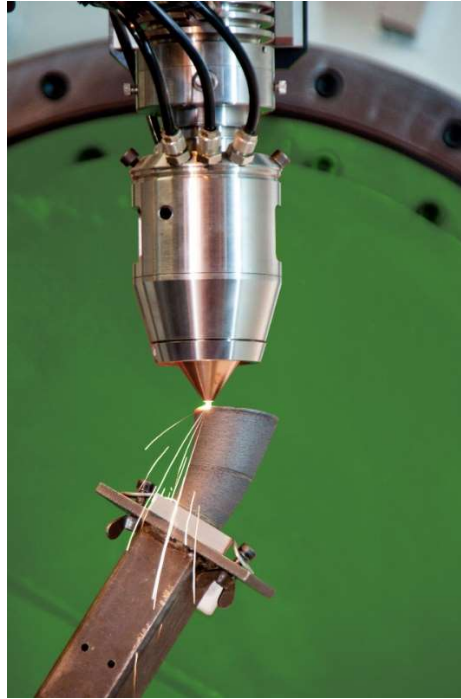


Figure 5 - LMD deposition process, with robotic control, application [20].

Another aspect that is important to mention is the fact that the process often uses an inert gas, such as argon, helium or nitrogen, which involves the molten pool. These inert gases are mainly used to prevent oxidation of the parts [16] during the solidification process.

One of the possibilities that powder LMD offers is the capability of creating personalised alloys, by mixing powders of different metals before they meet the laser beam that melts them into the molten pool. It should be noted, however, that some metallic powders might not combine, resulting in faulty deposited layers [16].

The quality of the final piece is highly connected with three main points, namely the laser power, the laser focus and the translation speed of the laser feed stock. As an example, a DLF process using a Nd-YAG laser, with a 0.5 mm focus, can produce solid layers with the thickness varying anywhere from 0.3 to 2.5 mm. Overall the accuracy is around ± 0.12 mm, with surface medium roughness of around $10 \mu\text{m}$ [16].

The usually high surface roughness is still one of the most difficult barriers to overcome, since the deposited layers form components with high surface roughness that prevents the direct use in an industrial application, meaning that near-net shape component manufacturing is still something that is not entirely developed and established.

2.2.1. Powder and wire LMD

The materials used in LMD are basically metallic powders or wires, which are usually obtained by powder metallurgy and by wire drawing, respectively, techniques that are significantly distinct in terms of complexity.

From the gathered bibliographical information, it is possible to conclude that powder LMD was the first form to be developed, however, this does not necessarily mean that wire LMD is a weaker process in terms of feasibility.

Wire LMD offers several advantages when compared to powder LMD, and several limitations as well.

Wire fed LMD is capable of applying high deposition rates, with few concerns about porosity, and it can overall be considered cheaper than the powder fed alternative. On the other hand, wire fed LMD encounters geometrical difficulties, not being able to deposit thin walls, overhangs and hollow structures. Another aspect is that wire LMD requires high heat input, ending up resulting in a high energy consumption ^[21].

Wire feed techniques also present some problems when using robotic control, not functioning properly with it. Dilution of the deposited material into the substrate is also high, with values close to 20%, against the 5% resulting from powder feed techniques ^[22].

Although wire fed techniques offer a nearly 100% efficiency of material usage, high energy rates are required, since lower values tend to prove to be insufficient to fully melt the wire and also because the wire shows high variations in energy absorption, resulting in defective depositions ^[23].

Additionally, wire feeding mechanisms have several significant limitations and are often unable of maintain a constant stream of wire to the laser focal zone, meaning that gaps and “valleys” could appear on the final component if the feeding process is done incorrectly ^[19].

On the other hand, powder LMD has several advantages, mostly linked with the component manufacturing itself, given that it offers the best design freedom out of both alternatives, the possibility of overhead deposition, the capability of working in large build volumes (when compared with similar AM techniques) and it is capable to produce new components and repair existing components, offering excellent surface mechanical properties .

One of the biggest limitation of powder LMD is linked with the manufacturing of the metallic powder, which is often associated with health concerns, mostly in the production phase, with high values of toxicity associated, ending up constituting a hefty advantage to wire feed alternatives, that have much less health concerns in its manufacturing ^[24].

The metallic powders used in LMD generally present better variety than the wire variant since the materials that can be reduced into to powder state are nowadays quite large.

However, some considerations should be taken into concern with the use of metallic powders such as the grain size that should vary between 50µm and 150µm ^[25]. These grain sizes are not however directly related to the thickness of the deposited layers, with the diameter of the laser focal point being the key feature in the determination of the layer thickness, which ends up representing one the main issues related to LMD, given that a large enough laser diameter needs to be assured in order to melt the metal powder. But at the same time, the larger the

laser diameter the larger the thickness and width of the deposited layer, resulting in a somewhat unsatisfying resolution on the final component [26].

2.2.2. Metallic wire

The process to achieve the metallic wire for LMD is wire drawing, which is a relatively simple process, similar to extrusion, with the difference being that the workpiece is pulled rather than pushed. The process is often cold performed and a cross section reduction is implied to the original metallic components through the use of a die [27].

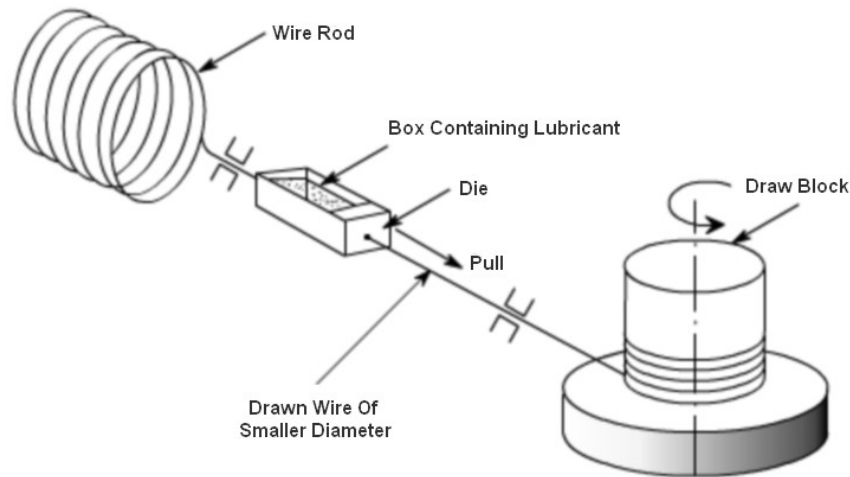


Figure 6 - Schematic representation of wire drawing [27].

Since wire drawing is performed by pulling the workpiece, it is possible that the yield strength is overpassed, which can result in yielding. This means that large cross section reductions may result in defects in the wire, with reductions of 15% to 45% being optimal to wire drawing.

The complexity of wire drawing machines can rise, if better mechanical quality is necessary on the wire, with several mechanisms being present to assure good wire properties.

Since it is necessary to imply a plastic deformation on the metal to draw it through the machine, there are a few limitations on the used raw material, however most metals are suitable for this application.

Regarding the use of wire in LMD processes, there are a few more aspects that must be considered. The laser beam used is essentially a heat and light beam and being a form of light wave it is prone to reflection when hitting a reflective surface [28].

Most metals are highly reflective, namely copper, brass, gold, silver and aluminium, being especially reflective, characteristic that stays with the metal when in wire form [29]. This means that the metallic wire may be defectively melted, resulting in a bad deposition, affecting the final component porosity, resolution, microstructure and overall mechanical quality.

Besides chemical composition, some properties like tensile strength, yield strength, elastic modulus, density, resistance to corrosion, thermal and electrical conductivity, among others, should be considered when selecting the material.

The variety of available metallic wires for the LMD process is large since that most metallic materials that are prone to welding can in fact be used, however, some materials may need an inert gas barrier or chamber in order to be used ^[30].

Amongst the most commonly used materials in wire LMD are AISI 316/316L stainless steel, Inconel 625 and Titanium 6Al-4V. All of these materials present a significantly lower price when in wire form rather than in powder form, with AISI 316 stainless steel costing 2.1 times more, Inconel 625 costing 2.1 times more and Titanium 6Al-4V costing around 2.4 times more ^[31].

Taking into account the mechanical properties and the overall cost of the materials, one of the metallic wires that offers a good quality over cost relations is AISI 316L austenitic stainless steel, which presents high corrosion resistance and high temperature strength, being often used in exhaust manifolds, heat exchangers, jet engine parts and other similar applications. Grade 316L also offers good chloride corrosion resistance due to the molybdenum present in its chemical composition and good chemical resistance ^[20].

2.2.3. Metallic powder

The other form of material used in LMD is metallic powder, which is produced just like mentioned before, through powder metallurgy, which unlike wire drawing is much more complex to perform.

Powder metallurgy represents a whole industry that aims to produce metallic powders, and the variety of different processes to produce them is broad, with four main processes existing, namely direct reduction, liquid atomization, gas atomization and more recently, centrifugal atomization ^[32].

Direct reduction, also known as sponge iron, is a technique where iron, or another metal, is directly reduced to small pellets of the metallic material, using a reducing gas or elementary carbon.

Gas atomization is a process where molten metal (alloyed or in pure form) is conducted through a small orifice under high pressure, into a gas filled chamber, where it will cool down, solidify and deposit inside the chamber.

Liquid atomization is like gas atomization, with a high-pressure liquid spray hitting the metal stream, which will then cool the metal stream, causing it to solidify and deposit in the form of small droplets.

Liquid atomization offers better powder quality, since the process uses a faster solidification of the metallic stream, which results in smaller and cleaner powder particles.

In both liquid and gas atomization, the deposited particles are collected and then they need to be annealed, for future industrial purpose.

The centrifugal atomization process uses a metallic rod inside a chamber and then placed inside a rotating spindle. An electric arc is then created across the gap to reduce the ends of the rods into powder, which then solidifies in small particles. Centrifugal atomization offers the advantage of being able to create a much smaller size distribution of the metallic powder particles.

Whichever process may be selected, there are a few aspects of the metallic powder that should be monitored, namely the flowability, the packing density and the level of contaminants [32].

Powder manufacturing techniques have several more concerns associated with it when comparing to the wire alternative, like health hazards and energy consumptions, among others. However, and despite these inconvenient, metallic powders offer better mechanical characteristics within the final produced parts and much better process control, with less limitations.

The range of metallic powders available is very broad since this process is applicable to most existing metals. However, there are a few metals that are more suitable to powder reduction, offering better mechanical characteristics.

Amongst the most common metallic powders being used are nickel based alloys such as Inconel 625, 718 and 738, Titanium based alloys such as Titanium 6Al-4V and Iron based alloys such as H11, H13 and AISI 300 and 400 series [33].

One of the materials that offers a good relation between quality and cost is AISI 431 stainless steel, capable of offering a good wear resistance, impact strength and the best corrosion resistance amongst martensitic stainless steels [34]. Thanks to these characteristics, AISI 431 stainless steel is often used to produce hard bearing parts, resist abrasive grains and hard surfaces and salvage grindable steels.

2.2.4. Laser technology

Laser technology is a key part of LMD since it is through it that the metal changes its state, from solid to liquid, making the whole deposition process possible.

The concept of laser, short for “Light Amplification by the Stimulated Emission of Radiation”, was first introduced in 1957 by Gordon Gould, who presented means of producing light, a stimulated emission, through excited atoms or ions.

The first laser was shown only in 1960, by Theodore Maiman who presented a pulsed ruby laser, which used high electrical voltages to create an explosion of light that would then excite the atoms in the ruby crystal, which in a determined state of energy are capable of emitting photons [35]. The concept is presented in figure 7.

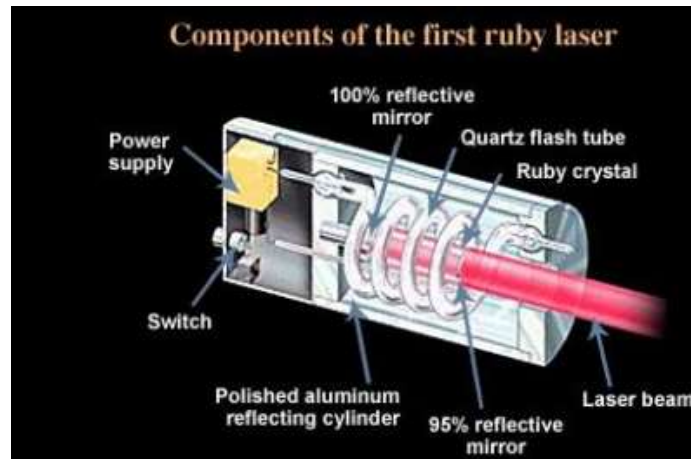


Figure 7 - Schematic representation of the first designed ruby laser ^[36].

Still in 1960, the concept of gas lasers was also presented, in the form of a helium-neon laser, which much like the ruby laser, used an electric discharge to stimulate the atoms and producing light. In addition, the first diode laser was also presented, with the same idea on the background, meaning that a diode is used to produce gain through the electrical current flowing, ending in a discharge of photons ^[35].

Much like the light from a common bulb, laser beams consist in a wave of electromagnetic radiation, with a defined, and constant wavelength, that can be located within the infrared, visible or ultraviolet areas, and it's formed by coherent light, with waves assuming the same direction and frequency, with constant phase between themselves, which allows one to predict the electric field of a point through another ^[35].

Unlike other forms of light waves, laser can propagate through long distances given the high intensity and the fact that the beam is well collimated.

The mean in which the stimulation is created can assume a solid, liquid or gas state, resulting in different types of lasers. However, there are mainly three types of laser that are most commonly used in most industries, namely:

- Semiconductor lasers: diode lasers are the most common within this category, that uses electrically or sometimes optically pumped means to produce light;
- Solid-state lasers: these are based on ion-doped crystals or glasses, pumped through discharge lamps or laser diodes, with the most common means of gain achievement being Nd:YAG, Nd:YVO₄, Nd:Glass, amongst others;
- Gas lasers: these typically used electrical discharges in order to excite the gas (commonly CO₂, Argon, or even gas mixtures, such as Helium-Neon).

Given the endless capabilities of laser technology, the applications are very broad, with several industries using this technology, such as the medical, textile, communications, military and entertainment, among many others.

Within LMD, the most typical lasers that are used usually belong to the solid-state group of lasers, such as disk lasers, diode lasers, fiber lasers, among others.

The tendency of solid-state laser usage in LMD was verified in the components manufactured by IK4-Tekniker, which were manufactured using a diode pumped Nd:YAG laser ^[39].

3. Materials and methodology

3.1. Experimental LMD components

The present work is based on the performance of LMD operations with different materials with the aim of its subsequent study. Since the technology under analysis is not available in the Polytechnic of Leiria, several contacts were made with companies, at the national and international level, that allowed the availability of test samples. Those contacts were established with several companies actively working with LMD technology, such as Trumpf and IK4-Tekniker.

This phase culminated with one of the mentioned organizations, IK4-Tekniker, providing several powder and wire LMD components that were produced in the aim of a previous feasibility study lead in the past by the company.

The IK4-Tekniker supplied several test samples, identified in red in Figure 8.



Figure 8 - Components produced by IK4-Tekniker and provided for analysis ^[37].

The provided components consisted in both powder and wire LMD components which were produced using roughly the same equipment, with minor changes to adapt for each form of LMD, but with distinct materials for each form.

The machine used to manufacture both the powder and wire LMD components consisted in a 2.2 kW diode pumped continuous wave Rofin DY022 Nd:YAG laser, with the laser beam being guided towards the work area through a 0.6 mm diameter fiber and an optical head from Precitec. The powder was injected into the molten pool area using a three-hole coaxial nozzle made by IK4-Tekniker. The movement of the laser head was implemented through a 6-axis ABB 4400 robot.

In both the powder and wire LMD cases a DIN C45E carbon steel substrate was used, with a thickness of 10 mm (typical properties in table 2).

Table 2 - DIN C45E typical main mechanical properties ^[38].

Material	Tensile strength [MPa]	Yield strength [MPa]	Elongation (% in 50 mm)	Brinell hardness [HB]
DIN C45E	670 - 720	340	15 - 18	170 - 240

The powder LMD components were manufactured using a Sulzer Metco Twin-10C powder feeder, with a feed rate of 15 g/min and a translation speed of the laser head stock of 400 mm/min.

During the deposition of the different provided components, different deposition heights were applied, between 0.3 mm and 0.9 mm, which resulted in components with different properties ^[39].

The referred “deposition height” consists of the distance set between the substrate onto which the material is being deposited and the deposition nozzle, which is determined by the point where the laser focal point and the material feedstock cross, resulting on the material melting.

The metallic powder used was Metco 42C martensitic stainless steel, which is similar to AISI 431 grade stainless steel.

This metallic powder is usually produced recurring to water atomization, a type of liquid atomization, offering an irregular powder morphology like it is visible in figure 9, with a nominal particle size distribution varying from -106 to +45 μm ^[40].

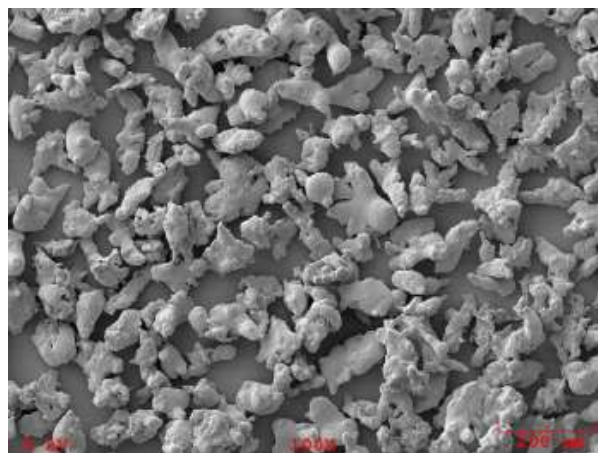


Figure 9 - SEM photomicrographs of Metco 42C metallic powder ^[40].

The composition of Metco 42C includes Iron (Fe), Chromium (Cr) in 17 % nominal weight, Nickel (Ni) in 2 % nominal weight and Carbon (C) in 0.18 % nominal weight ^[34].

The typical properties of Metco 42C are shown in table 3.

Table 3 - Metco 42C (equivalent to AISI 431 Stainless Steel) typical mechanical properties ^[34].

Material	Tensile strength [MPa]	Yield strength [MPa]	Elongation (% in 50 mm)	Brinell hardness [HB]	Density [Kg/m³]	Elastic modulus [GPa]
Metco 42C - AISI 431	940	750	19	280	7700	200

The wire LMD components were also produced under the same conditions presented above, with the exception that the layer height was kept constant, at 0.9 mm, given the morphology of the process. The laser power was also lowered to 1.5 kW, unlike the translation speed of the laser head stock, which was raised to 1200 mm/min. The wire feed rate was of 3 m/min, using a different mechanism than the one used for the powder feed.

The metallic wire used was AISI 316L austenitic stainless steel, produced through wire drawing.

The composition of the AISI 316L steel shows high rates of Iron, Chromium (16-18 %), Nickel (10-14 %), and includes Molybdenum (2-3 %), Manganese (2-3 %), Silicon (0.75 %), Nitrogen (0.10 %), Phosphorus (0.045 %), Carbon (0.03 %) and Sulphur (0.03 %) ^[41].

The typical properties of AISI 316L are shown in table 4.

Table 4 - AISI 316L Stainless Steel typical mechanical properties ^[41].

Material	Tensile strength [MPa]	Yield strength [MPa]	Elongation (% in 50 mm)	Brinell hardness [HB]	Density [Kg/m³]	Elastic modulus [GPa]
AISI 316L	570	300	40	165	8000	193

Both types of components were produced using an overlap between consecutive layers of 40 % of a single bead width, which in this case should represent a value of 1.3 mm. Each layer consists of an external perimeter deposition, followed by a zig-zag trajectory that ends up filling the inner section ^[37].

The layer width for the powder components should be of about 3.2 mm.

Although most of the obtained parts were represented in figure 7, there were a few which were not shown.

The entirety of the provided components, as well as their dimensions, and identification, are presented in figures 9 to 11 and figures 13 and 14.

It should be noted that powder LMD components have a “ Px ” identification, with the “ P ” standing for the powder variant, and “ x ” being the number identification of the component in no specific order. The wire components on the other hand, have a “ Wx ” identification, with the “ W ” standing for the wire variant, and the “ x ” standing for the number identification, again, in no specific order.

The five powder LMD components are presented below (Figs. 10-12), as well as the deposition strategy used to produce them (Fig. 13).



Figure 10 - Component P1 (left) and P2 (right) originally provided by IK4-Tekniker.

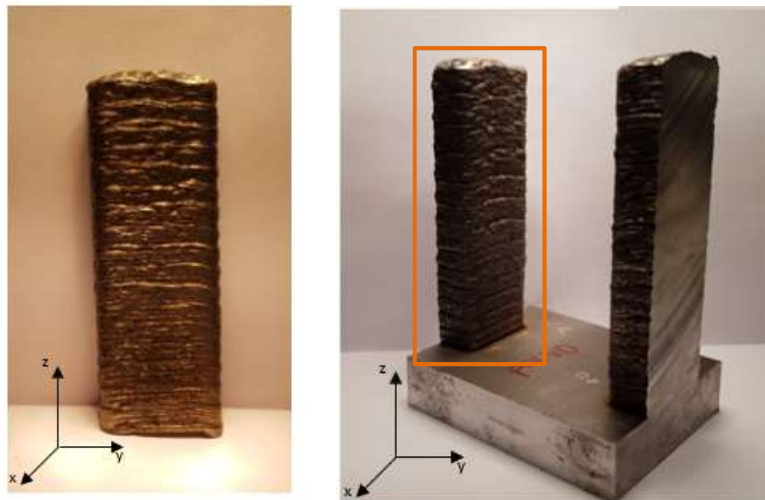


Figure 11 - Component P3 (left) and P4 (right) originally provided by IK4-Tekniker.

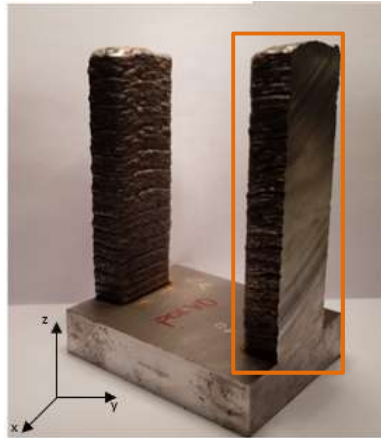


Figure 12 - Component P5 originally provided by IK4-Tekniker.

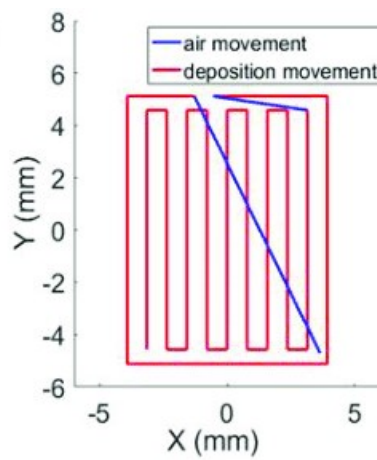


Figure 13 - Deposition strategy for the base, which is repeated on the z-axis, overlaying layers, creating the final powder components ^[39].

Table 5 presents the dimensions of the components shown in figures 10 to 12, as well as the deposition height used, which is determined upon the deposition process.

Table 5 - Powder LMD components dimensions (x, y, z).

<i>Number identification</i>	x [mm]	y [mm]	z [mm]	Deposition height
<i>P1</i>	12.55	28.05	78.80	0.3
<i>P2</i>	13.45	29.00	79.00	0.9
<i>P3</i>	11.10	27.00	77.50	0.8
<i>P4</i>	13.00	26.20	80.00	0.7
<i>P5</i>	13.00	27.50	78.70	0.8

The five wire LMD components are presented below (Fig. 14-16), as well as the deposition strategy used to produce them (Fig. 17), which is similar to the one used on the powder components.

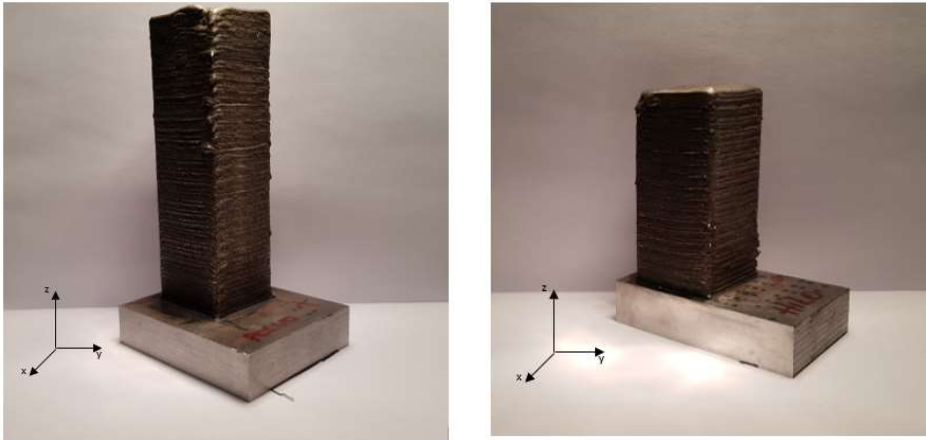


Figure 14 - Component W1 (left) and W2 (right) originally provided by IK4-Tekniker.

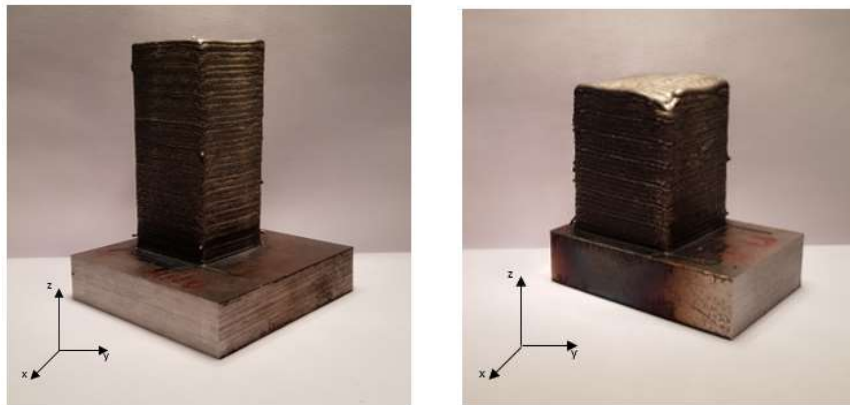


Figure 15 - Component W3 (left) and W4 (right) originally provided by IK4-Tekniker.

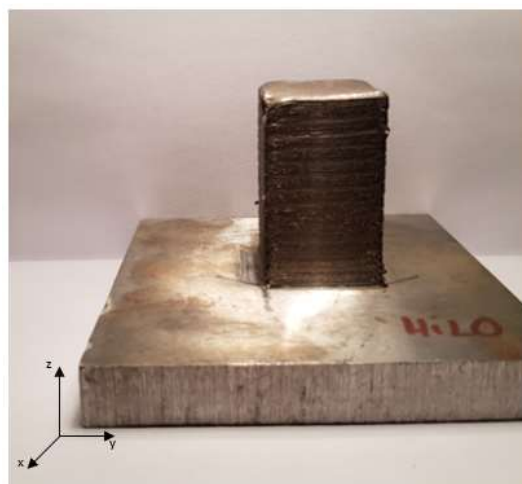


Figure 16 - Component W5 originally provided by IK4-Tekniker.

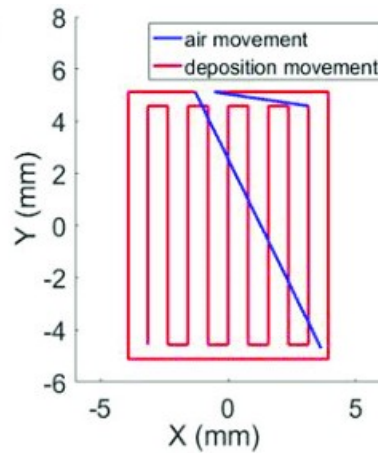


Figure 17 - Deposition strategy for the base, which is repeated on the z-axis, overlaying layers, creating the final wire components ^[39].

Table 6 presents the dimensions of the wire components, as well as the deposition height used, which in the case of the wire LMD components, is 0,9mm for all the components given the morphology of the process itself.

Table 6 - Wire LMD components dimensions (x, y, z).

<i>Number identification</i>	x [mm]	y [mm]	z [mm]	Deposition height
<i>W1</i>	30.60	30.60	99.00	0.9
<i>W2</i>	30.60	30.90	60.00	0.9
<i>W3</i>	30.50	30.90	62.10	0.9
<i>W4</i>	30.30	30.90	37.90	0.9
<i>W5</i>	31.00	30.75	47.35	0.9

3.2.Component preparation

In order to be able to perform further mechanical tests some type of processing had to be done to the components available.

Firstly, the substrate had to be separated from the components themselves, to isolate the deposition base from the deposited material.

Secondly, the parts were processed in a way that an acceptable surface finish was achieved, taking away from the parts the bumps and ridges created by the deposition process.

These bumps and ridges represent one of the biggest limitations of both powder and wire LMD, which leads to a poor surface quality, preventing the direct use of components in an industrial application, and usually requiring further surface treatment to achieve an acceptable surface finish.

Consequently, it is possible to understand that the dimensions that the parts present after processing them into a more acceptable surface quality, are slightly smaller than the ones presented in table 5 and 6, which refer to a rough shape, just as they are produced.

The first preparation procedure step was similar to the powder and wire LMD components, and consisted on the separation of substrate from the deposition material. The selected equipment for this process was a manual cut-off machine, more specifically a Struers Labotom-3 (Fig. 18).

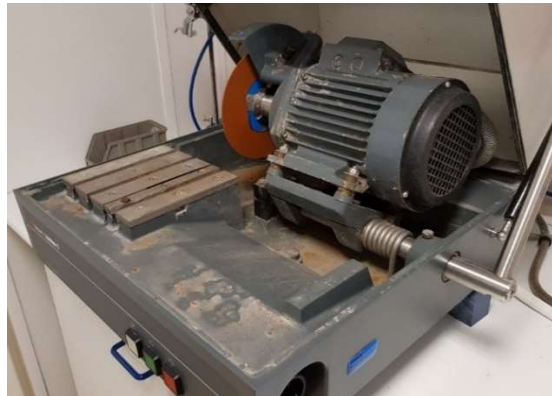


Figure 18 - The equipment Struers Labotom-3 used to separate the deposited material from the substrate.

The result of this process is a separation between the substrate and the deposited material, with a loss of about 1 to 2 mm of material on the z-axis.

In some cases, due to the grooves and ridges present in the surface of the components, as well as the equipment limitations, the cut could not be made exactly in the separation between the two parts, leading to a bigger material loss. However, the surface on which the cut was made presents good surface finish, with minor signs of the cutting disk passage.

Figure 19 presents the surface of both the substrate and the deposited material surface after the cut, for a wire and a powder component.

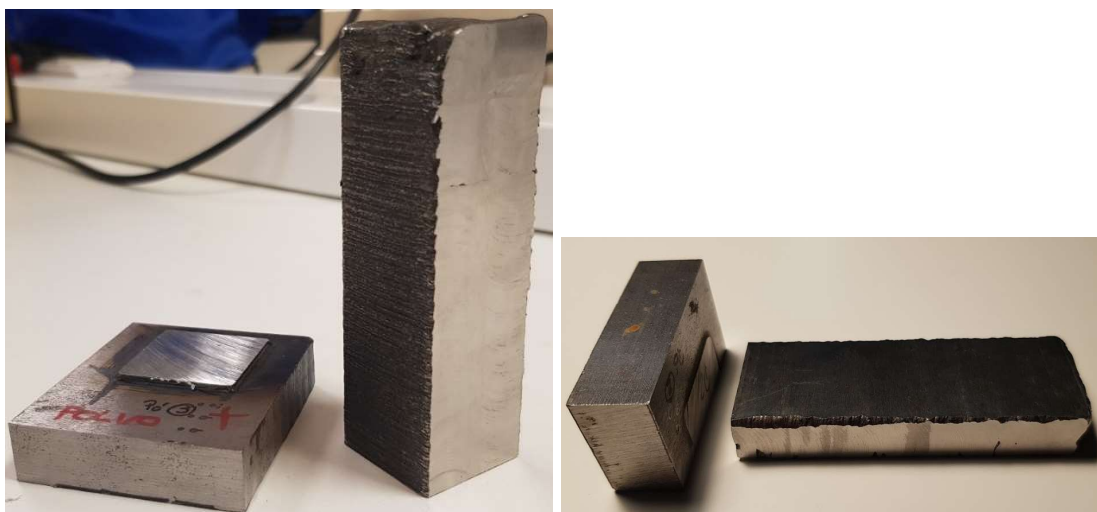


Figure 19 - Representation of a wire (left) and powder (right) component after the separation between the substrate and the deposited material.

With all of the components separated from their substrate, surfaces with a poor surface finish were grinded or milled, depending on their magnetic behaviour.

On the powder LMD components, given the presence of magnetism, a precision surface grinder was used. The used machine, a Chevalier Falcon FSG-3A818, operates by grinding the surface with increments of 0.02 mm in height, leaving behind a good surface finish.

During the process, an effort was made to maintain a continuous lubrication of the components in order to prevent heating effects on material, however some small marks appeared on some of the components. Despite this fact, the areas to be evaluated presented no marks whatsoever.

Regarding the wire LMD components, given the lack of magnetism, a turret milling machine was used, more exactly, a Holke F-10-V machine. This machine also allows the control of the z-axis displacement, allowing increments of 0.1 mm.

The result is a piece with good surface finish, but not as good as the precision surface grinder used on the powder components, since there are visible mill passage marks.

With the test components preparation completed all of the components were in a state that allowed the planning of the experimental tests.

3.3. Methodology

The methodology used to perform the mechanical characterization of the LMD components was built in a way that allowed to maximize the amount of information obtained from each available component, while taking into consideration both the timeframe and the available equipment.

The first mechanical tests to be conducted were the ones that required less component processing, using the components as close to their original state, and the final tests were the ones that required the most component processing.

This also ends up meaning that the first mechanical tests tended to have a non-destructive nature, and subsequently, the last tests tended to have a destructive nature.

Before conducting any of the selected tests the surface had to be prepared given the heavily scratched finish that all of the components showed after the preparation process described in chapter 3.2.

A graphical representation of the timeline of methodology followed for the experimental work is presented in Fig. 20.

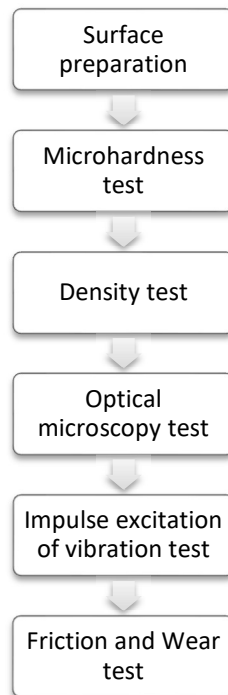


Figure 20 - Graphic representation of the conducted mechanical tests, in a timeline.

The first stage was the surface preparation of the test components. This first task was performed before all of the selected mechanical tests were done, in order to assure a good and scratch free surface.

The first mechanical test to be conducted was the microhardness test, a non-destructive test, which was selected given that it offers data that helps to clarify how the components relate to the reference values for the material in which they were manufactured.

The following test was the density test, also non-destructive, requiring however a cut of a small piece on the transversal plan. Density testing was selected given that it clarifies the existence of porosities on some level and allows the comparison of the component's material with the same material processed through conventional techniques.

The third selected test was an optical microscopy test, also non-destructive, which used the same small pieces obtained for the density test, requiring further polishing in order to obtain a finer scratch-free surface. Optical microscopy testing allows the understanding of the arrangement of the layers, as well as the visualisation of the material microstructure.

The fourth test was the impulse excitation of vibration test, which is again of a non-destructive nature, but required the cut of a thin rectangular slice (ratio of width to thickness being between 20 and 25) of the component on the vertical axis. This test was one of the last ones to be conducted. This test was selected due to the mechanical properties that it is capable to determine, allowing a good characterization of the components.

Finally, the last test to be conducted was the friction and wear test, the first one of a destructive nature. This test required the cut of small thin pieces that were cut from the slice

used on the impulse excitation of vibration test. This test was selected given that it allows to understand the behaviour of the components under a specific set of conditions, which ends up offering data that can be used to predict how a component produced with this material would behave under real work conditions.

With the methodology schedule defined, each individual stage is now presented in the following chapters.

3.3.1. Surface preparation

In order to eliminate the scratching an incremental process was carried out, where several sandpaper grit sizes were used to eliminate scratches and imperfections, and also to take any hints of oxidation. The sequence of the process is presented in figure 21.

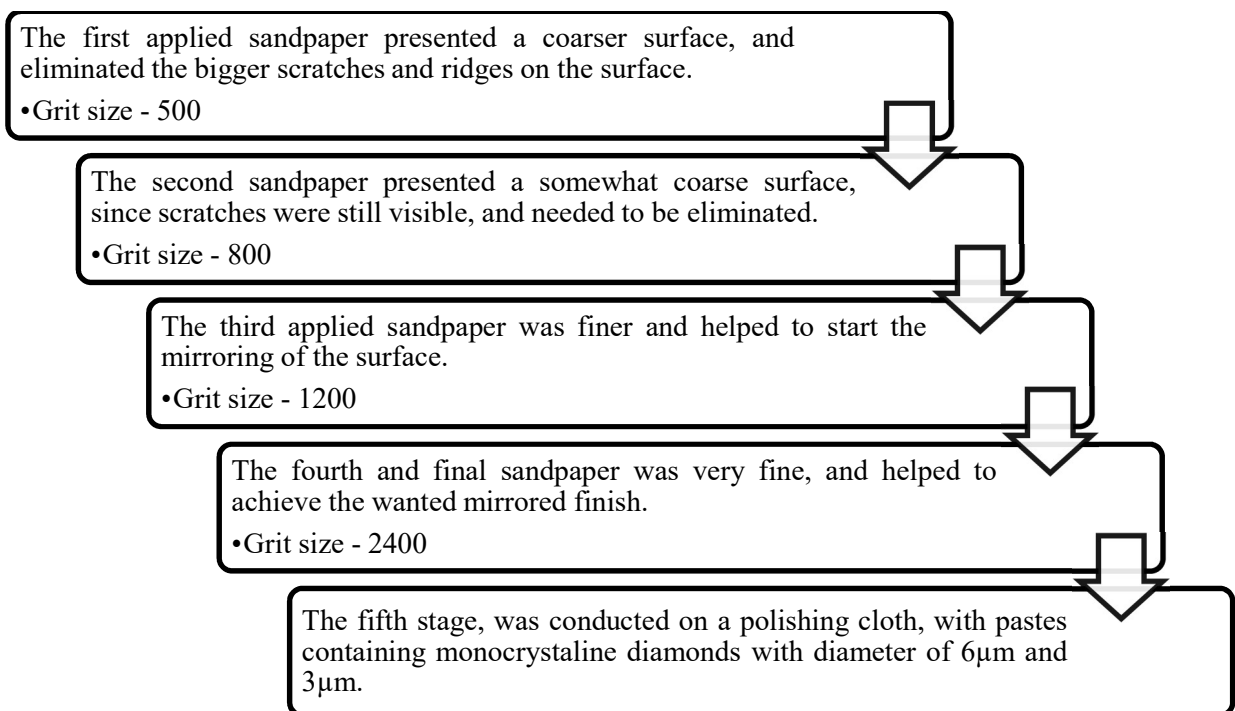


Figure 21 - Surface polishing preparation process.

Some of the used ASTM standards alert to the fact that heating effects during grinding and work-hardening during polishing, should both be avoided. To counteract on this, water was used during grinding, and a specific lubricant was used during polishing to maintain low temperatures.

The machine used to grind, using sandpaper, and polish, using a polishing cloth, the components was the Struers RotoPol-21, which uses 25 mm diameter sandpaper and cloth disks, and rotates with a speed of either 150 or 300 rpm. The machine also allowed the automation of the process, holding specimens in a chamber that is able to rotate and apply a constant normal force of 5 or 10 N, during a previously set amount of time.

The first four stages described in figure 21, consisted on the use of four different sandpaper grit sizes and was conducted on the left plate of the polishing machine visible in figure 22.

After the first four stages of sanding, during the fifth stage, the components were polished on the cloth surface on the right side of the polishing machine, also visible in figure 22.



Figure 22 - The Struers RotoPol-21 equipment, the polishing machine used to prepare the components for microhardness testing.

3.3.2. Microhardness test

Hardness testing can be classified into several categories, with them being macrohardness, microhardness and nanohardness.

Despite the form of hardness test in question the goal is always the same, which is to determinate a material resistance to a permanent plastic deformation, through the penetration of another harder material [42].

It is important to understand that hardness testing does not offer a material's fundamental property, which means that the results should be evaluated in a quantitative manner, taking in account aspects like the load applied by the indenter, the time this load is applied and the geometry of the indenter.

Given the properties of the material in test and the morphology of the manufacturing process leading to a component with a fine microstructure, non-homogeneous and prone to cracks and fissures, the macrohardness test is not the most suitable to evaluate the variation of the hardness throughout the component, since it is expected that the value varies significantly from one point of the component to another.

The most accurate and enlightening test that suits the methodology and that can offer a good representation of the hardness throughout the component, is the microhardness test. This test offers a good idea of the variations that occurs given the presence of microstructures and the high temperatures that the material reaches when components are produced, that result in different surface characteristics [43].

In order to evaluate microhardness variations on the components, ASTM E92 [44] standard was used. The equipment used to perform the tests was the Shimadzu HMV-2, available at the ESTG facilities, which is designed specifically for Vickers microhardness testing.

This standard contemplates the determination of Vickers microhardness of metallic materials, using loads that range from 1 to 120 kgf.

An important point that the standard states out is that for practical purposes, the Vickers hardness number is considered constant when a load of 5 kgf or higher is used. At lower loads, the Vickers hardness number may be load dependent ^[44].

Despite this fact, a load of 4.903 N (0.5 kgf) was applied, with an application time of 15 seconds.

The results of the standard application are materialized on the calculation of the Vickers hardness number, which is related to the applied load and to the surface area of the permanent impression made by a square-based pyramidal diamond indenter with faces angled in 136°.

The standard also refers the need to prepare the surface before conducting any kind of testing, given that the test specimen surface should allow the visualization of the diagonal ends in a clearly defined way, with a 0,5 μm precision.

A preliminary microscope observation, under the 40x ampliation lens of all of the available components revealed a surface with some evidences of scratching, as shown in figure 23, which prevented the necessary precision when measuring the diagonals, pointing the need for further surface preparation.

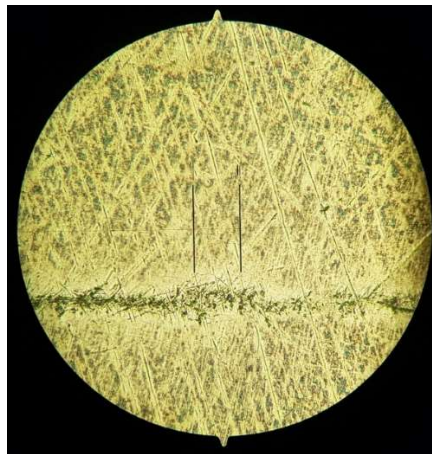


Figure 23 - Representation of a bad surface finish, with too many scratching, due to bad polishing.

After obtaining the desired surface finish, through the process described in chapter 3.3.1, the test components were ready to be put through the microhardness test.

Regarding test specimen shape and dimension, standard does not present any requirement apart from the need to secure the test specimens in order to avoid any kind of rocking or shifting during testing. As for thickness, it should be enough to avoid the bulge or marking showing the effects of the applied load on the opposite side of the specimen ^[24].

An illustration of the indenter's geometry, as well as the indentation and its diagonals, are presented in figure 24.

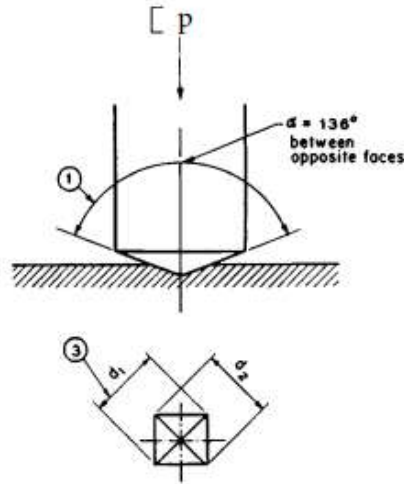


Figure 24 - Vickers hardness test ^[44].

The indentation was observed with a 40x ampliation lens, and diagonals (d_1 and d_2) were measured with the equipment above mentioned. The ideal indentation and an example of the test indentations are presented in figure 25.

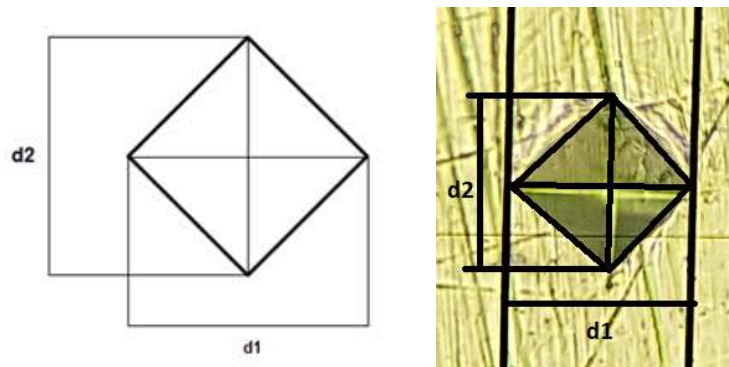


Figure 25 - Comparison between the ideal indentation (left picture) and a real indentation (right picture).

The microhardness value is calculated using the applied load and the average value of the resulting diagonals (d_1 and d_2), through equation (1).

$$HV [kg/mm^2] = 0.1891 \cdot \frac{F}{d^2} \quad (1)$$

A strategy that allowed to define the measurement position variation throughout the vertical axis of the components was created. Tests were conducted from a point located near the top of the components, where the last layers were deposited, to a point near the base of the components, where the first layers were deposited. Figure 26 illustrates the methodology used to measure the micro hardness throughout the component.

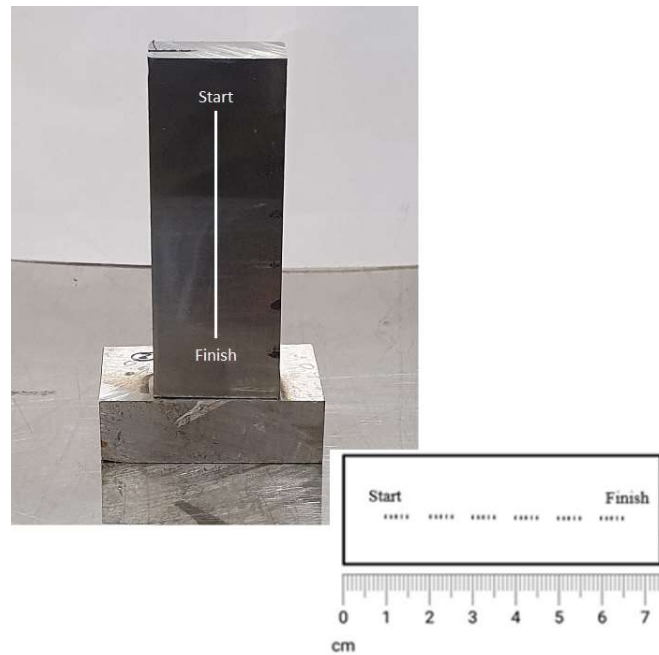


Figure 26 - Representation of the area subjected to the microhardness Vickers test.

The referred strategy consisted in measuring the microhardness value in groups of 5 points, with 1 mm between points of the same group, and 10 mm between the first point of every group, resulting in a clear representation of the measurement position variation throughout the entire component.

The used machine is equipped with a table, that allowed movements in the transverse plane, with a resolution of 0.1 mm, allowing a precise distance between the points of measurement.

All of the powder LMD components (P1, P2, P3, P4 and P5) were subject of the microhardness test, given that all of them present different deposition height, as for the wire LMD components, only one of them was subjected to microhardness testing, given that all of them present the same deposition height, and the same production parameters, disregarding the need to test all of them.

Given that the opposite face of the components was somewhat irregular, it was necessary to mount the components on a clamp, in order to guarantee that the surface to be tested was perfectly perpendicular to the indenter.

3.3.3. Density test

Through relative density testing, the relation between a components mass and volume is achievable, which, alongside the reference value for the material density, allows the understanding of how compact a component is, demonstrating any gaps or cracks on the components structure.

However, and despite this fact, the conducted density testing is only applied to a small portion of material, with a mass of typically around 5 g, which means that the results have

to be interpreted with this in mind, because any major gaps that could be present on the component could not present themselves in this specific test.

This test was not conducted under any specific standard, and used a Mettler Toledo AG204 scale, with an apparatus like the one presented in figure 27.

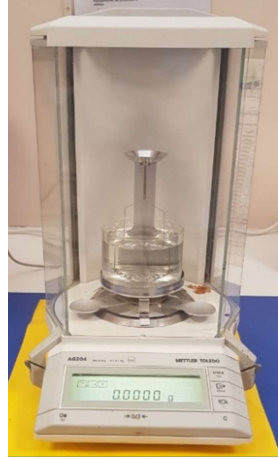


Figure 27 - Density testing apparatus.

The test consists in two weight measurements of the component, one in dry condition and another in submerged condition, which then allowed the calculation of the density of the component, through equation (2).

$$d_{component} = \left(\frac{m_{dry}}{m_{dry} - m_{submerged}} \right) \cdot d_{H_2O@T_{air}} \quad (2)$$

In order to conduct the density test, given the size restriction implied by the equipment (mass ideally between 1 and 10 g), a small piece had to be cut from the components. Figure 28 presents the piece cut from each powder component, and although it is not presented, the wire piece was similar.

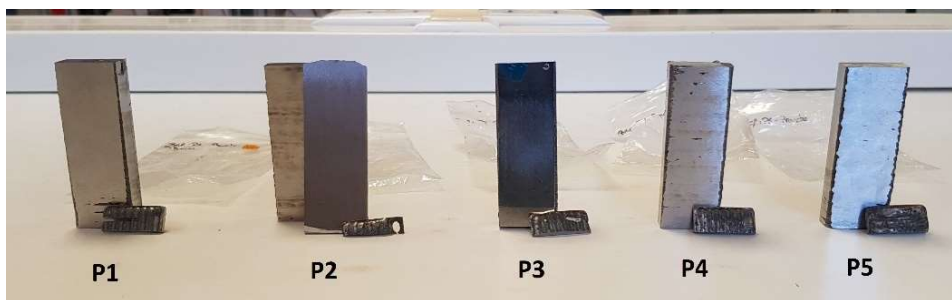


Figure 28 - Detail of the cut components for density testing.

3.3.4. Optical microscopy test

Optical microscopy testing is an excellent way to visualize and analyse the microstructure of a metallic specimen and is capable of offering a good understanding of how a production process affects final components.

Microstructure on its own has a strong influence on the properties and successful application of a metallic component [45], indicating its importance, and therefore, the importance of analysing it on the components in hand for this project.

Adding to the fact that a metallographic analysis can offer a representation of the state of the microstructure on the components, also the layer arrangement can be visualized with a lower magnification.

For optical microscopy testing only components P2 and W2 were selected since these were the only ones that were later subject to impulse excitation of vibration, and friction and wear testing. Despite the fact that both test components were produced using two different forms of LMD, the distance set between the substrate and the deposition nozzle was 0,9mm for both cases, making these two components the most appropriate pair to compare wire and powder forms of LMD.

Despite the existence of ASTM standards for the preparation of metallographic specimens, the available equipment did not allow the strict following of any standard. However, the followed preparation process was thorough in order to achieve acceptable results.

The specimen holder had a circular shape with 29.8 mm of diameter, meaning that the specimen shape itself had to follow under this restriction. Both a powder and wire sample were cut from components P2 and W2, respectively, like presented in figure 29.



Figure 29 - Detail of the small pieces cut from components W2 (on the left) and P2 (on the right) for the optical microscopy test.

After performing the cut, the specimens were ready to be mounted on a holder using the Struers Acryfix hot mounting kit. The positioning procedure of samples was followed, and the resin was left to cure for 24 hours, before starting the surface preparation process.

With the resin totally cured, the following process was related with the surface preparation, given that the smoothest possible surface, with a scratch free mirrored finish needed to be achieved, while assuring minimal deformation.

This imposed an intense grinding process, with several sandpaper grit sizes being used in an iterative manner, followed by a polishing process that also used several diamond polishing pastes with iterative grit sizes.

For the grinding process, Struers silicon carbide grinding paper was used, with a combination of grit sizes of 220, 500, 800, 1000, 1200 and 2400, using water as a lubricant, and a rotation speed of 150 rpm. These were used on a Struers RotoPol-21 machine, with a Struers

RotoForce-1 arm, in order to guarantee that constant even pressure was applied (5 and 10 N) to the specimens to achieve the best results.

As for the polishing process, the same machine setup was used, with a DP-Dur cloth disk, and two diamond pastes, both Struers DP-Paste M, with the first having a 6 μm grit size, and the second having a 3 μm grit size. In both cases DP-Lubricant was used. For the polishing process a load of 5 N was used with a rotation speed of 150 rpm.

The result was the desired finishing, without any visible scratches, just like presented in figure 30.

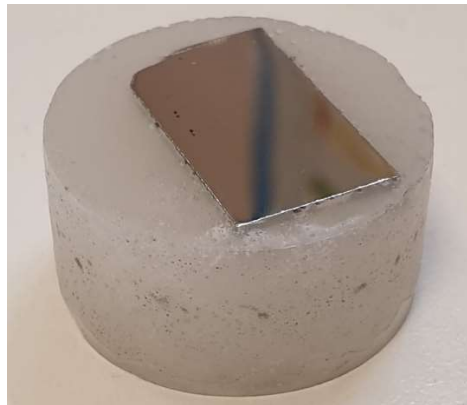


Figure 30 - Detail of the specimen mirrored surface finish.

With the surface preparation phase completed, the next stage, before analysing the specimens under the microscope, was etching the surface in order to enhance the separation between layers and the microstructure.

For the powder specimen (P2), made with AISI 431 martensitic steel, the selected etchant was “Kalling No. 2” (left in table 7), which is indicated for martensitic steel [46]. As for the wire specimen (W2), made with AISI 316L austenitic steel, the selected etchant was “Carpenter Etchant” (right in table 7), which is indicated for austenitic steel [47].

Table 7 - Chemical composition of the used etchants for component W2 (left) [46] and P2 (right) [47].

Kalling No.2	Carpenter etchant
12 g Copper (II) Chloride (CuCl_2)	8.5 g Iron (III) Chloride (FeCl_3)
20 ml Hydrochloric Acid	2.4 g Copper (II) Chloride (CuCl_2)
225 ml Ethanol	122 ml Hydrochloric Acid
	122 ml Ethanol
	6 ml Nitric Acid

The powder specimen was immersed on the solution for 5 seconds, and the wire specimen was immersed for 10 seconds.

3.3.5. Impulse excitation of vibration test

Mechanical elastic properties such as Young's modulus, Shear modulus and the Poisson ratio, offer a good representation of the mechanical profile of a given component, which follows the main goal of the present project.

As such, and continuing to follow the line of non-destructive tests, given the low availability of test specimens, a mechanical vibration test was selected to obtain such properties.

The test was conducted under ASTM E1876-01^[48] standard, and allowed to determine dynamic Young's modulus, Shear modulus and Poisson's ratio through means of impulse excitation vibration, not damaging the test component in any way shape or form.

This test method allows the determination of the mentioned mechanical properties at ambient temperatures, given that the materials in which the components are produced have specific mechanical resonant frequencies that are determined by the specimen's elastic modulus, mass and geometry.

The measurement of these fundamental resonant frequencies is made by mechanically exciting the component with a singular elastic strike using an impulse tool.

A transducer is then used to sense the resulting mechanical vibrations of the component, transforming them into an electric signal that is later analysed in order to obtain the fundamental resonant frequencies.

This test method is often used for material characterization, and is preferably applicable to materials that are elastic, homogeneous, and isotropic, which is presumably the case of both the wire and powder LMD components available.

However, it should be noticed that the results can sometimes be considered not satisfactory in cases where the specimens present major discontinuities, such as large cracks or voids. While this is not the case of the tested LMD components, small cracks and voids were observed, indicating that the components could present a rather high porosity.

The apparatus to conduct this test (graphical representation in fig. 31) consists of 4 parts: the impulser, which applies the exciting impulse by lightly striking the specimen with a suitable implement; the signal pickup, which as the names indicates is responsible to pick up the vibration signal by means of a transducer; the electronic system, which consists of a signal conditioner/amplifier, a signal analyser and a frequency readout; and a support system, that is responsible to isolate the specimen from any external vibrations without restricting it from the desired mode of vibration.

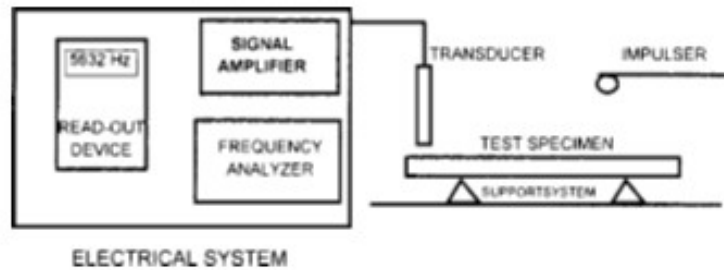


Figure 31 - Mechanical vibration test apparatus ^[48].

The test specimen should be subject to preparation in order to present either a rectangular or circular cross-section, with a ratio of width to thickness of 5 or greater, with the optimal ratio being between 20 and 25.

Both a wire LMD component (W2) and a powder LMD component (P2) were tested in order to understand the differences between them and to understand how both compare to reference values of the obtained mechanical properties.

Just like presented in chapter 3.3.4, the reason for the selection of components W2 and P2 lies on the fact that despite both being produced using two different forms of LMD, the distance set between the substrate and the deposition nozzle was 0.9 mm for both cases.

3.3.6. Friction and Wear test

The final conducted test, and the first to be considered destructive, was the friction and wear test, which is a test capable of offering a clearer idea of how a material behaves under specific environmental conditions, with the possibility to reproduce operating conditions such as temperature, fluid interactions, direction of wear, amongst others.

The wear test results, unlike the previous tests, offer a better understanding of the behaviour that the components would have in a specific environment, given that the conditions at which the test is conducted are able to emulate those of a real-life situation.

Additionally, the test is also capable of offering friction data, with the characterization of the friction coefficient throughout the entire test.

However, it should be noticed that the results do not allow to determine the component's material fundamental properties but instead, the perspective of a specific component behaviour under a specific set of environmental conditions, allowing a comparison between different components under the same wear conditions.

The selected wear test has a reciprocating nature, and it allows a variation in the amplitude of movement and in the normal load value, which ends up giving the possibility to emulate several test conditions that better characterize a real application of a component produced with the technique under analysis ^[49].

This test was designed and performed in ICEMS – University of Coimbra, and although it does not follow any specific standard, it is well developed and capable of simulating true to life conditions, allowing an evaluation of contact wear in both materials under testing.

The used geometry of contact was a ball to plane, with the ball (number 7 in Fig. 32) in the form of a zirconium sphere with 10 mm diameter (properties in table 8), being connected to the moving stage (number 2 in Fig. 32), which is in permanent contact with the stationary horizontal plane (number 4 in Fig. 32), in the form of both LMD components.

Table 8 - Zirconium sphere mechanical properties ^[50].

	Density [kg/m ³]	Young's modulus [GPa]	Friction coefficient	Hardness HV
Zirconium oxide sphere	6000	210	0.2	1043 - 1446

The normal load is applied by a spindle-spring (number 5 in Fig. 32), which is then connected to the normal load cell (number 1 in Fig. 32), that measures the normal load applied, which was varied between 3, 5 and 7 N. The horizontal movement of the zirconium sphere is generated by an eccentric-and-rod mechanism set with stroke length of 2 mm, and frequency of 3 Hz, imposes the referred reciprocating movement of the upper sphere carrier. The lower specimen holder, where the LMD components were placed, is connected to a ball linear bearing slider, in order to allow movement in the direction of the sliding reciprocating motion. The stationary load cell (number 3 in Fig. 32) is used to equilibrate the lower specimen holder attaining the friction force values along the test.

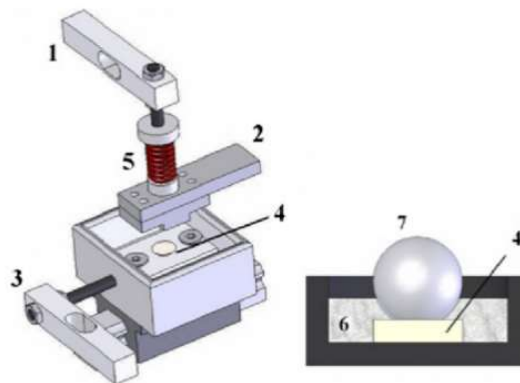


Figure 32 - Wear testing apparatus ^[51].

Result analysis, on the stationary plane side (LMD samples) is made by measuring the depth of the wear track, to calculate its area, to then multiply it by the wear track length, obtaining the volume that was stripped away from the surface.

On the other hand, the results regarding the sphere are evaluated differently, given that it is possible to measure directly the scar diameter on it.

The procedure contemplates the measurement of the diameter in two orthogonal directions, one along the motion direction and another in the direction perpendicular to the motion, and then using these two values to calculate the average radius. Combining the average radius (r) and the original radius (R), it is then possible to obtain the depth (h) and volume (V) of the wear track created during the test, by using equations (3) and (4). Finally, and using the depth and volume of the wear track, it is then possible to calculate the wear rate (k), using equation (5).

$$h = r - \sqrt{R^2 - r^2} \quad (3)$$

$$V = \frac{\pi}{3} \cdot h^2 \cdot (3R - h) \quad (4)$$

$$k = \frac{V}{F \cdot L} \quad (5)$$

The equipment also allows to obtain the evolution of the friction coefficient throughout the time of the test and also a graphical representation of the geometrical profile of the wear track.

These tests were performed on components W2 and P2, produced by wire and powder LMD respectively, both presenting a deposition height of 0.9 mm.

The selected components were tested under several wear conditions, under the values of normal force of 3, 5 and 7 N, and both the upper portion (last deposited layers) and the lower portion (first deposited layers) of the components were tested.

All of the wear tests conducted consisted of 1800 reciprocating cycles that ended up in a sliding distance of 7200 mm.

The friction and wear tests were performed at 24 °C of temperature and 35 % of humidity.

4. Results and discussion

Having finished all the experimental procedures defined in the methodology introduced in section 3.3, the results are presented and discussed in the following sections.

4.1. Microhardness test

Through the application of the methodology described in chapter 3.3.2, a profile of microhardness for each component was obtained, allowing the identification of tendencies and average values.

From Figure 33 to 35 are presented the profiles of microhardness throughout the vertical axis of each tested component.

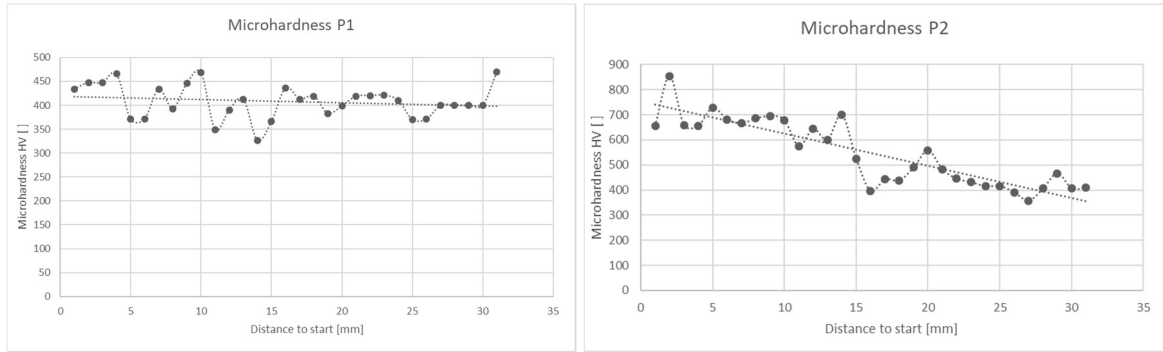


Figure 33 - Microhardness test results for components P1 (left) and P2 (right).

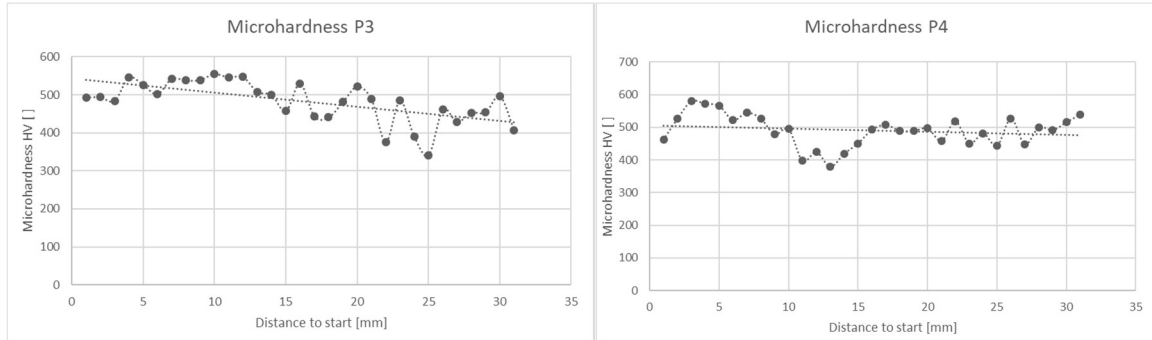


Figure 34 - Microhardness test results for components P3 (left) and P4 (right).

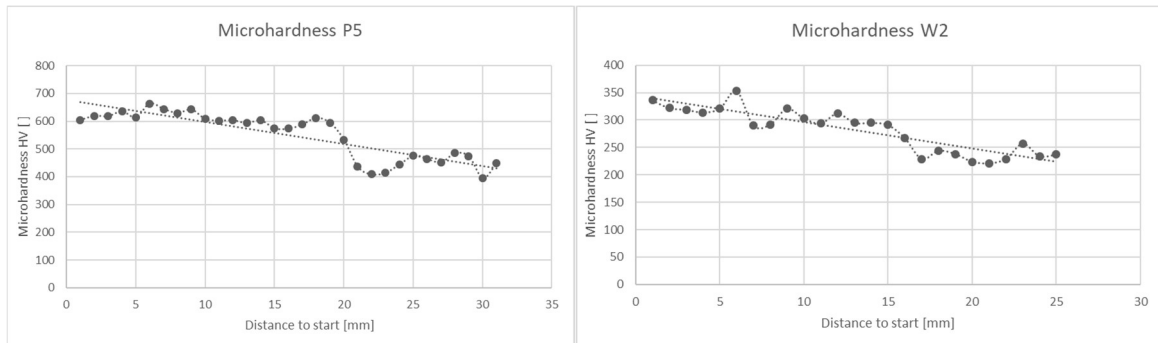


Figure 35 - Microhardness test results for components P5 (left) and W2 (right).

Through the analysis of the data, it was possible to calculate the maximum, minimum, and mean value of microhardness in each component, as well as the standard deviation, with all of these presented in table 9.

Table 9 - Microhardness test results.

	Max HV	Min HV	Mean HV	Standard deviation
P1 (0,3 mm)	470	327	408	35.07
P2 (0,9 mm)	854	358	547	132.52
P3 (0,8 mm)	555	341	483	54.59
P4 (0,7 mm)	580	380	490	48.87
P5 (0,8 mm C.C.)	663	396	550	83.82
W2 (0,9 mm)	353	221	281	39.96

Regarding the powder components, the results indicate that the higher the deposition height, the higher the value of the mean microhardness, a tendency that is also reflected on the maximum and minimum values. This indicates that the distance set between the substrate and the deposition nozzle affects the microhardness of the components produced with powder LMD.

A possible explanation could be that as the deposition distance grows, despite the fact that the molten pool diameter is presumably larger, its depth is presumably smaller, this should translate in a faster solidification process, ending up generating the higher values of microhardness.

The smaller depth of the molten pool, also means that as a layer is deposited, the layer that is immediately below it, should not be as re-melted as it would be if a smaller deposition height was used, subjecting the already deposited layers to less significant melt and re-melt cycles.

The overall results are higher than expected, since the reference values point towards a hardness on the 300 HV range ^[34], and the lowest registered on the conducted test was of 408 HV, which is still significantly higher. However, the process of deposition could explain this fact, given that the material is put under severe thermal cycles and other conditions that are likely to induce an increase in microhardness.

As for the wire component that was tested, the mean value for microhardness was also higher than expected, given that the reference value is of 160 HV ^[41], and the one registered on the conducted tests was of 281 HV. The same explanation could apply here, given that the process of deposition puts the material through thermal cycles that alter the microstructure that can in fact translate in a higher value of microhardness.

Through this data, it was also possible to determine the tendency line, which is defined by an equation of the type $y(x) = mx + b$, where m is the slope of the curve. In this particular case, the higher the value of m in modulus, the greater the variation of the microhardness from the start to the end of the tested area.

The graph presented in figure 36 shows the value of the tendency line slope for all the tested components, as well as the standard deviation that was already presented in table 9.

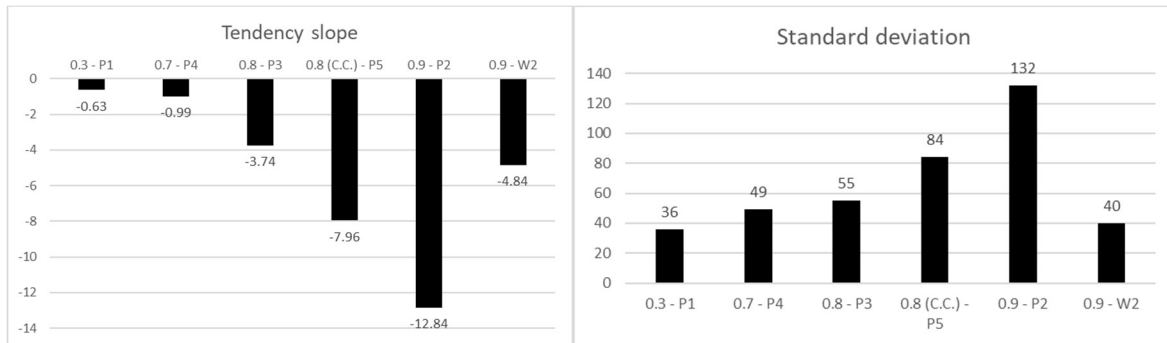


Figure 36 - Graphical representation of the relation between the deposition height and the microhardness tendency line slope (left) and standard deviation (right).

On the graphical representation of the tendency slope, it is possible to observe that it acquires a negative value for all of the tested components, showing that there is a clear tendency to register higher values of microhardness towards the top of the components (last deposited layers), and subsequently, lower values towards the bottom (first deposited layers), which means that microhardness decreases from top to bottom.

A particularity of the graphs shown in figure 36 is that, rather than presenting the data in the order through each component was tested, the presentation is done in order to present first the lower deposition heights and last the higher deposition heights, for the powder components, since there is only one component of the wire variant.

Through this, it becomes clearer that there is a tendency, showing that the higher the deposition height, the higher the slope of the microhardness tendency line, and also the higher the standard deviation.

This shows that there is a relationship between the deposition height and the magnitude of variation between the top and bottom portions of the components, in such a way that the higher the deposition height, the higher the modulus of the tendency line slope, and subsequently, the higher the difference between the microhardness values registered on the top of the component and on the bottom of the component.

This tendency could be explained through the cooling process that occurs in each layer, which starts immediately after it is deposited. The layers towards the bottom are deposited firstly and begin a slower cooling process given that the subsequent layers are being deposited, and the temperature on this region of the component is kept relatively high, for a longer period of time, affecting the cooling rate, a situation that changes on top of the component, since these layers will have a different cooling rate process, cause no further layers are being deposited on top, allowing a much more efficient cooling process.

Additionally, it should be noticed that in some of the cases of the powder LMD components, some of the used deposition heights were lower than usual, which could lead into an abnormal deposition and cooling process, thus affecting the microhardness of the

component, since the layer that is being deposited could merge into the layer that was deposited below, meaning that some layers could be re-melted and suffer several thermal cycles.

Another important issue is the standard deviation that registers throughout the several deposition heights tested. It is possible to identify a tendency that shows that the higher the deposition height, the higher the standard deviation (right graph in figure 36), which indicates that an increase of this parameter (deposition height) translates into a higher difference between the microhardness registered on the top of the component and on the bottom of the component.

The conclusions that were drawn from the standard deviation analysis lie on the fact that there seems to be a clear relation between the standard deviation and the tendency line slope, meaning that higher values of standard deviation are a direct translation of the variation of microhardness that occurs from the top to the bottom of the specimens, and not connected with error on the testing process.

However, the relation between the standard deviation and the tendency line slope, is something that should be noticed. There are major variations of microhardness in the tests, which were expected considering the small volume of material deformed to achieve the microhardness values. This wide variation on microhardness values is a result of the LMD process, which often implies different cooling rate in different layers and also the influence of built material porosity.

To corroborate the microhardness results, further tests should be applied to the manufactured components, such as a macrohardness test, which would help to evaluate the standard deviation variation on the microhardness results.

4.2.Density test

The results regarding density are expectedly lower than the reference value for wrought material, given that in the process of preparing the components to the impulse excitation of vibration and wear tests, wire electro discharge machining was attempted, in order to cut a thin vertical slice from each component, a process that failed to perform the cut, presumably, due to the high porosity of the parts that ended up creating a short circuit, making the cut impossible.

Following this line of thought, it is then expected to see a relatively high porosity come clear on the density results.

The test was conducted using deionized water, at 20 °C, with a corresponding density of 0.99882 kg/m³.

The mass of the components in dry and submerged state, as well as their density is presented in table 10.

Table 10 - Density test results.

Component	Mass in dry condition [g]	Mass in submerged condition [g]	Density [kg/m ³]	Variation from reference ^[34, 41] in %
P1	6.1624	5.3570	7637.58	2.08% lower
P2	2.5869	2.2486	7633.00	2.14% lower
P3	5.6374	4.8938	7567.58	2.98% lower
P4	7.9109	6.8726	7606.01	2.49% lower
P5	9.8348	8.5472	7624.34	2.25% lower
W2	6.4175	5.6157	7989.46	0.01% lower

Looking at the powder LMD components (P1, P2, P3, P4 and P5) produced with Metco 42C, similar to AISI 431 martensitic stainless steel, the reference value for density is around 7800 kg/m³, a value somewhat higher (around 2 %) than the one registered in the density tests, a tendency that is most likely due to the high porosity.

However, much like presented on the test description (chapter 3.3.3), the results only represent a small portion of the test pieces, and not the entirety of them. Larger gaps that are located in specific locations, interlayers of LMD parts, spots where is possible to develop gaps, would not be necessarily visible in this form of density testing.

Regarding the wire LMD component, made with AISI 316L austenitic stainless steel, the tendency is different and the registered value is approximately the same as the reference for the material in question, which indicates a lower value of porosity, almost without gaps and cracks.

However, some visible gaps were also observed on these components, and additionally, wire electro-discharge machining also failed to perform the cut on the wire LMD components. The fact that this presumable high porosity is not reflected on the results, could be due to the mentioned fact, that density testing only evaluates a small portion of a component, with the possibility of leaving major gaps undetectable.

Some of the gaps identified with an eye inspection, after cutting the components both on a vertical and horizontal axis, indicating that the overall density of the components can in fact be lower than the one resultant from the applied test, are presented below (figs. 37 and 38).



Figure 37 - Identifiable gaps on component W2, after performing a vertical cut.



Figure 38 - Identifiable gaps on component W2, after performing a horizontal cut.

4.3. Optical microscopy test

The optical microscopy test had two main goals, just as mentioned in chapter 3.3.4. The first one was to observe the layer dimensions and geometrical organization, and the second was to observe the microstructure itself.

Both the goals were achieved, and some conclusions can be taken. The results are presented below with several pictures that were obtained.

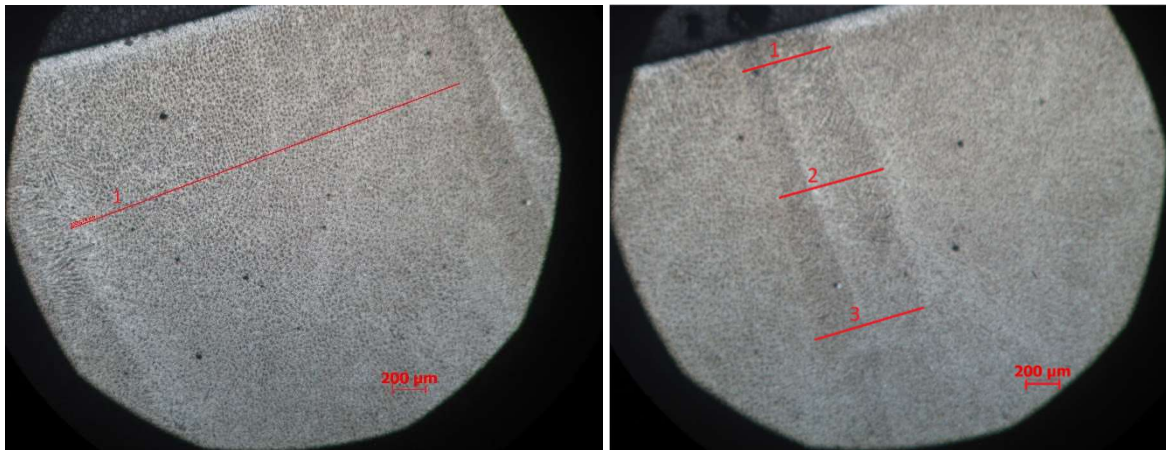


Figure 39 - Single layer disposition (left) and horizontal layer overlap (right) on component P2.

On component P2, the layer disposition was perfectly visible, and very well arranged, with the layers being parallel between themselves, and presenting similar dimensions on every visible layer.

In figure 39, on the left side image, it is possible to identify a dimension (line 1), that points the layer width. The registered dimension shows a width of around $2530 \mu\text{m}$, however, it was possible to observe a variation on the layer width as it approached its end, where the deposition head makes a turn on the deposition strategy, with this width becoming slightly smaller as the overlap dimension seemed to become larger towards this layer end point.

Still in figure 39, on the right side image, it is possible to identify a tendency, connected to the overlap between two layers, with its width being larger towards the end of each layer. The registered dimensions show that the horizontal overlap varies from $540 \mu\text{m}$ on line 1, to $624 \mu\text{m}$ on line 2 to $704 \mu\text{m}$ on line 3.

The results show that the layers tend to present a total width in the neighbourhood of 3.2 mm, which follows the theoretical data gathered in chapter 3.1, much as the overlap which in total represents around the 1.3 mm, also as presented in chapter 3.1.



Figure 40 - Layer disposition, with evidence of possible gap formation on component P2.

In figure 40 it is possible to visualize the arrangement between layers on component P2, showing that a gap is created in an area where no material is deposited. This could be irrelevant, due to the fact that, as the layer that is directly deposited above the one visualized presents a different orientation, being horizontally rotated by 90 degrees, the new layer should fill the gaps, however, as the production process occurs, some of these gaps could stand, causing higher values of porosity.

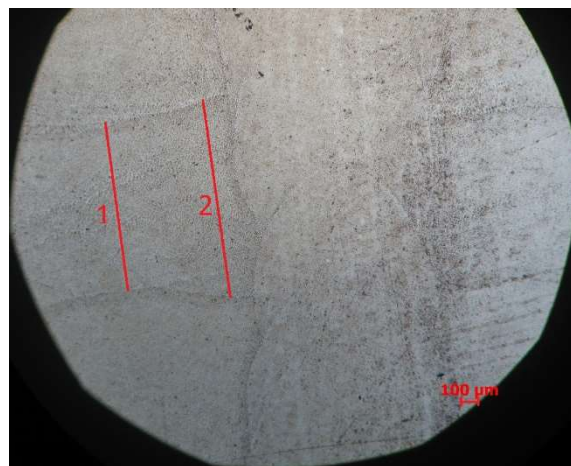


Figure 41 - Layer disposition on component W2.

As for component W2, the way that layers are arranged was perfectly visible. However, the layer arrangement was not as perfect as on component P2, with the layers not being parallel between them. In some areas of the specimen, it was possible to identify small parts of layers with a different orientation, being 90 degrees horizontally rotated, indicating that the area that was observed was most likely a result of a cut in the region of transition between layer.

Despite this fact, in some areas, it was possible to identify a geometrically well-arranged set of layers, making possible to understand how the width varies. The tendency observed on

component P2 repeated itself, with a single layer presenting a variation in width towards its end, however, in this case, the overlap was not identified, and the layer presented a larger width towards its end, rather than a smaller width as it occurred on component P2, which can be observed in figure 41. The registered dimensions show that the layer width varies from 944 μm on line 1 to 1177 μm on line 2 (both in fig. 41).

As for the overlap, as it was already mentioned, during the observation of the specimen, it was impossible to identify any sort of overlap region. This does not mean that the component was not produced using horizontal overlap, it possibly means that the material fuses in a way that the overlap is not visible.

Another important aspect observed lays on the fact that the gaps identified on component P2 were not visible on component W2, indicating that the layer construction could have less impact on porosity.

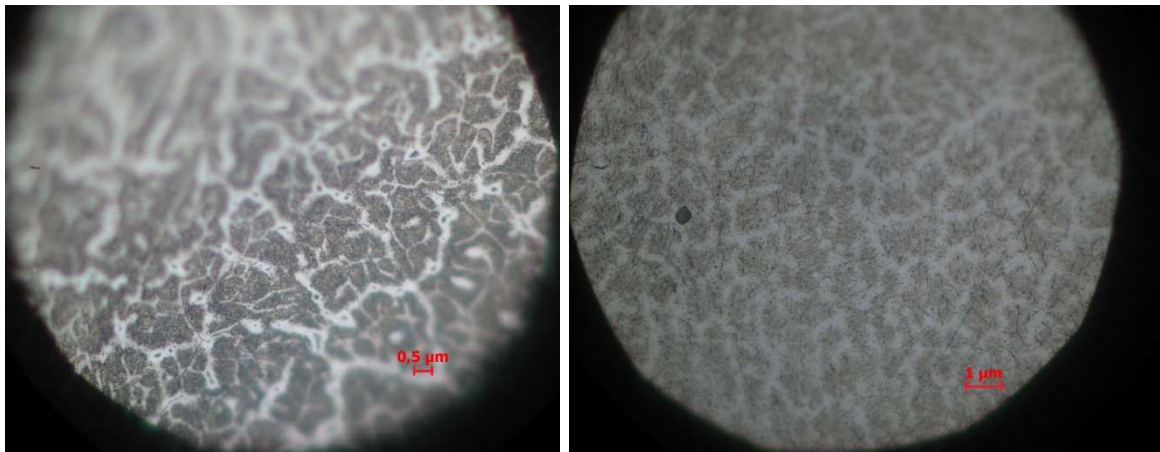


Figure 42 - Component P2 (left) and W2 (right) microstructure.

Analysing the microstructure itself, it is possible to observe in figure 42 that both of the components presented a very well arranged microstructure, with the grain size showing a consistent size, with component P2 (on the left of the image) presenting a mean grain size of 1.2 μm , and component W2 presenting a mean grain size of 1.1 μm .

The fact that the microstructure is well arranged corroborates the good mechanical properties that the components present.

4.4. Impulse excitation of vibration test

To achieve the necessary geometry of the test specimens for the impulse excitation of vibration test imposed by the standard, both components were cut, like mentioned in chapter 3.3.5.

Component W2 ended with a length of 54.4 ± 0.22 mm, a width of 17.84 ± 0.026 mm, a thickness of 1.77 ± 0.12 mm and a mass of 12.80 g. With this data, the value of density for component W2 was calculated, presenting a result of 7542 kg/m^3 .

Component P2 ended with a length of 52.42 ± 0.017 mm, a width of 27.08 ± 0.007 mm, a thickness of 1.63 ± 0.05 mm and a mass of 17.17 g. With this data, the value of density for component P2 was also calculated, presenting a result of 7446 kg/m^3 .

Figure 43 shows both the experimental and analytical vibrational waves that originate when W2 specimens were subject to an elastic strike, with a representation of the amplitude of vibration behaviour over time. Similar result was achieved for P2 component.

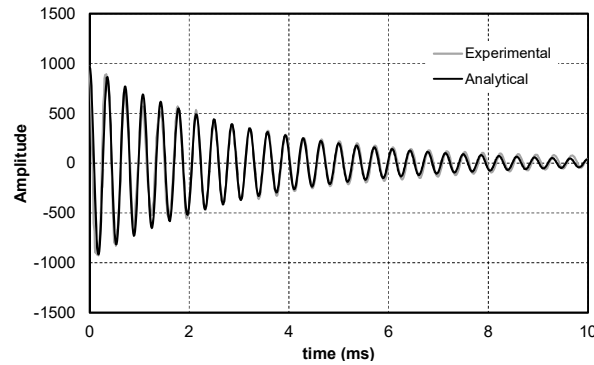


Figure 43 - Experimental and analytical response to the impulse excitation of component W2.

Through the representation of the vibration amplitude over the frequency, it is possible to visualize the fundamental resonant frequency, since the highest amplitude is registered within the area of said frequency, much like it is visible in figures 44 and 45, with point “1” being the first mode of bending and point “2” being the first mode of torsion, both obtained by the excitation in different directions.

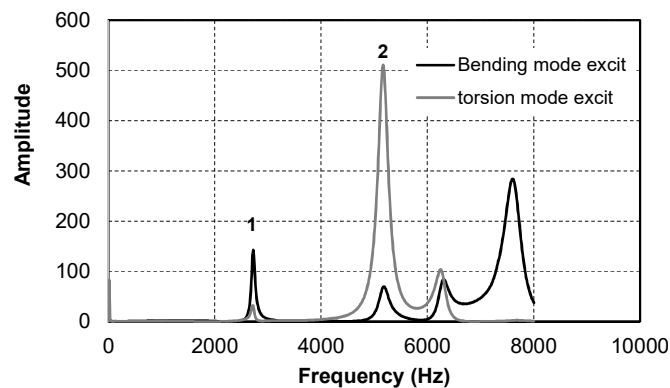


Figure 44 - Vibration spectra of component W2.

For component W2 the frequency at which the first mode of bending is registered is of 2722 Hz and the one at which the first mode of torsion is registered is of 5177 Hz.

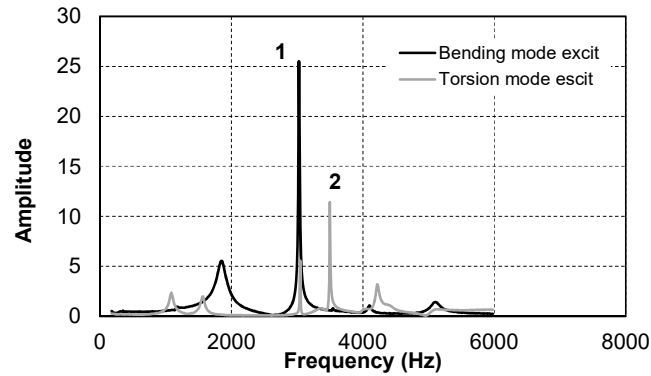


Figure 45 - Vibration spectra of component P2.

For component P2 the frequency at which the first mode of bending is registered is of 3029 Hz and the one at which the first mode of torsion is registered is of 3499 Hz.

With the values presented in figure 44 and 45, the mechanical properties were then calculated, and the results are presented in table 11.

Table 11 - Mechanical elastic properties, obtained through impulse excitation of vibration testing, for components W2 and P2.

Component	Young modulus [GPa]	Torsion modulus [GPa]	Poisson ratio
W2	146.00 (24.35 % lower than reference ^[41])	63.60 (17.40 % lower than reference ^[41])	0.15 (50.00 % lower than reference ^[41])
P2	192.28 (8.44 % lower than reference ^[34])	75.38 (3.26 % higher than reference ^[52])	0.275 (equal to reference ^[52])

When comparing the results of component W2 to the reference values for AISI 316L austenitic steel, it is possible to understand that the properties are significantly lower. This means that the process used to produce this part affects the final mechanical properties significantly, with a worse than normal mechanical behaviour being predictable.

As for component P2, the results show less variation when compared to the reference values, with lower than reference values only for Young modulus, higher than reference values for the torsion modulus, and equal to reference Poisson ratio value for AISI 431 martensitic steel, meaning that the mechanical behaviour of the component should be relatively similar to the one presented by a part produced through conventional methods with this material.

The variations between values for mechanical properties could be supported by the different density values that were calculate during the impulse excitation of vibration test (table 12).

Table 12 - Relation between density for components W2 and P2

Component	Density [kg/m ³]		
	Reference values ^[41,52]	Density Tests [Chapter 4.2]	Impulse Excitation samples
W2	8000	7989	7542
P2	7700	7633	7446

The density values that were obtained during this test, show that the density is significantly lower than expected, both from the reference values and the values obtained in density testing.

The results corroborate the hypothesis that the components do have a high porosity, since their density is significantly lower, with component W2 presenting a density 5.7 % lower than the reference, which represents a difference of around 458 kg/m^3 , and component P2 presenting a density 3.3 % lower than the reference, which represents a difference of around 254 kg/m^3 .

Also, the variations registered can originate in some aspects like the thermal cycles suffered by the component during manufacturing as well as the deposition process itself (deposition strategy as well as the translation and deposition speeds), which end up affecting the material microstructure and the porosity (and density of material) and thus affecting the elastic properties.

4.5. Friction and Wear test

Just like presented in chapter 3.3.6, wear test offers both wear data and friction data. The first data under analysis is the friction coefficient variation throughout the time of the test.

The following images (Figs. 46-47) present the variation of friction coefficient, distinguishing the top and bottom parts, for component W2.

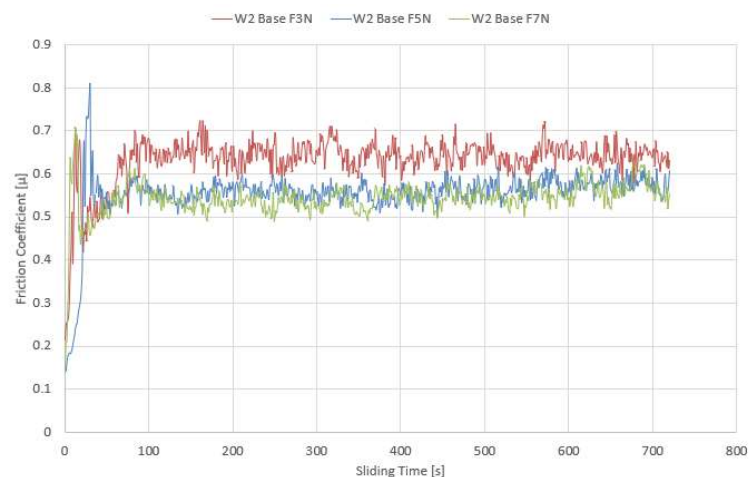


Figure 46 - Component W2 base friction coefficient variation during reciprocating sliding tests.

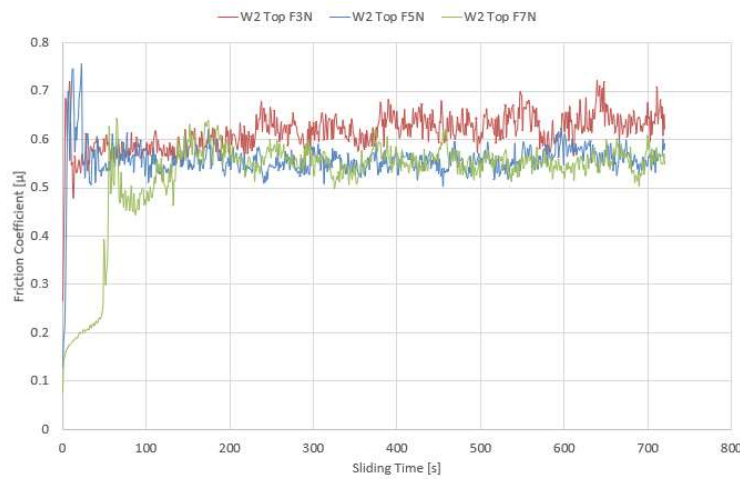


Figure 47 - Component W2 top friction coefficient variation during reciprocating sliding tests.

According to the friction test results for component W2, it is possible to understand that there is a visible relationship between the values of the friction coefficient and the normal load applied to the component during the test, both on the upper and bottom part of the components.

This relationship is proven in such a way that when friction coefficient attains a steady state regime, which occurred sensibly within the first 100 seconds of the test, the mean value of friction coefficient was higher for lower normal force values.

This relation could be due to wear, since the increase of the load translates in an increase of wear, thus removing a larger quantity of material from the component, that is most likely being deposited inside the generated crater and possibly creating a tribofilm that provides better sliding conditions between the bodies in contact, ending up reducing the friction coefficient.

Looking at the variation of the friction coefficient over time, it is possible to identify an initial phase with running-in effect where this coefficient rises rather quickly, until it stabilizes in throughout the rest of the test, at values around the 0.5 and 0.7 range.

It should also be noticed that the differences in the friction coefficient observed between the upper and lower part of the component are not significant, only verifying that the measured friction coefficient at the beginning of the test was slightly higher in the case of the lower part of the specimen, however the differences are minimal and do not allow conclusions to be drawn on this aspect.

Looking into component P2, the following images (Figs. 48-49) present the variation of friction coefficient also distinguishing the top and bottom parts.

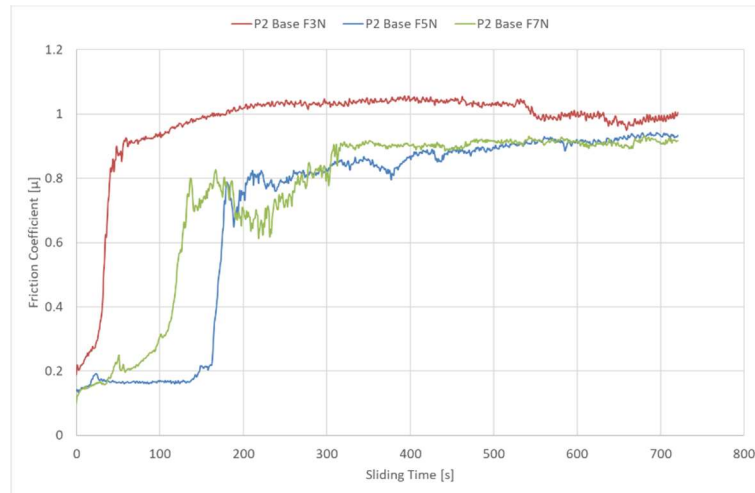


Figure 48 - Component P2 base friction coefficient variation during reciprocating sliding tests.

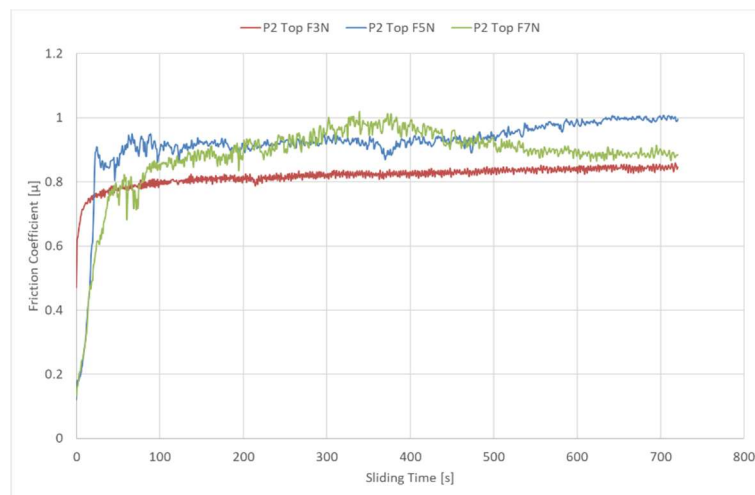


Figure 49 - Component P2 top friction coefficient variation during reciprocating sliding tests.

Regarding the friction test results for component P2, the relationship between the values of the friction coefficient and the normal load applied to the component during the test is not as clear as on the W2 results.

It is possible to understand that the behaviour of the friction coefficient through time follows a tendency for all the variations tested, with an initial running-in phase where the coefficient rises until it reaches a steady state regime, staying relatively constant during the rest of the test.

However, unlike the W2 component, here the steady state phase is somewhat less stable, with some test conditions showing some variation of friction coefficient.

This difficulty of stabilization could be connected to the higher microhardness present on the component P2, and to the fact that during the test, the removed material, was presumably being deposited directly into the cavity that was being created, but instead of forming a tribofilm, like on the case of the W2 component, it started forming compounds, and affected the sliding conditions negatively.

This is corroborated by the fact that on the end of the test, rather than observing a distinct cavity, some protuberances were observed, formed by the material that was being removed from both the specimen and the zirconium sphere.

It should be noticed that on the bottom part of the component, the value of friction coefficient fluctuated around 0.8 and 1, during the steady state phase. As for the top part of this component, the value of friction coefficient also fluctuated around 0.8 and 1 on the more stable phase, however, the overall picture, shows that the bottom part tended to go towards bigger values of friction coefficient.

Closing the friction coefficient analysis, a clear conclusion can be drawn, and it stands on the fact that the normal force applied does not influence the friction coefficient in a significant manner.

Having analysed the friction data, the following step is to evaluate the wear data, which can be split in two parts. The first links with the wear scar left on the zirconium sphere, which plays the ball part on the used ball-to-plane geometry. The second links with the plane part of the specified geometry and is evaluated through the wear track left on the LMD components.

The wear scars left on the zirconium sphere were observed with the aid of a microscope and registered (table 13 for component W2 and table 14 for component P2) so they could be measured using an image measurement software (Digimizer and ImageJ).

Table 13 - Wear scars left on the zirconium sphere for component W2.

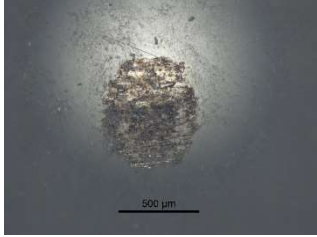
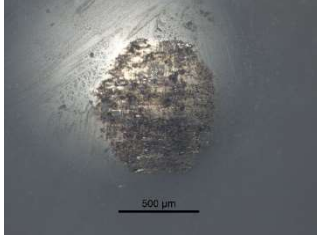
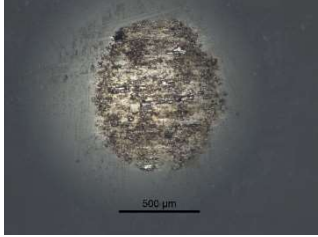
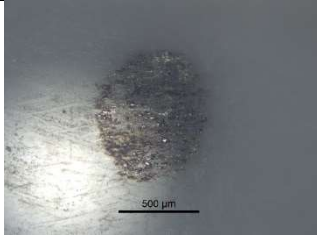
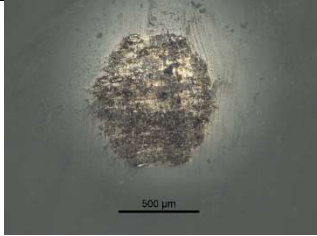
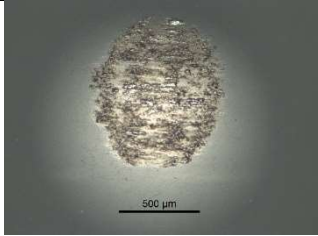
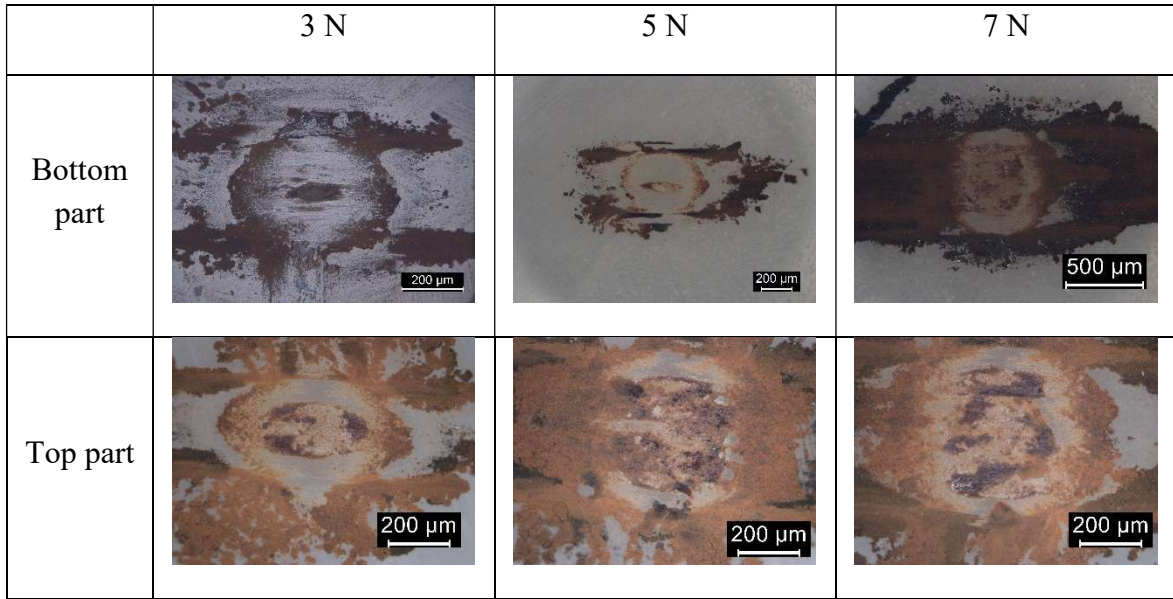
	3 N	5 N	7 N
Bottom part			
Top part			

Table 14 - Wear scars left on the zirconium sphere for component P2.


To achieve the wear rate coefficient, the diameter of the sphere needs to be measured firstly, to then calculate the depth and volume of the wear track, thus having all the necessary data to calculate the wear rate.

Table 15 and 16 present the measured diameters on the zirconium sphere, on both the test regarding component W2 and P2, respectively, that are then used to calculate the depth (h) and the volume (V) of the wear scars, using equations (3) and (4), and also the wear rate through equation (5).

Table 15 - Zirconium sphere wear scars diameters, depth (h) and volume (V) of the wear scars, and wear rate (k) of the component W2.

	$F_N = 3 \text{ N}$	$F_N = 5 \text{ N}$	$F_N = 7 \text{ N}$
Bottom part	$d_1 = 597.41 \text{ } \mu\text{m}$ $d_2 = 688.32 \text{ } \mu\text{m}$ $h = 10.34\text{e-}3 \text{ mm}$ $V = 16.78\text{e-}4 \text{ mm}^3$ $k = 7.8\text{e-}5 \text{ mm}^3/\text{N.m}$	$d_1 = 752.43 \text{ } \mu\text{m}$ $d_2 = 820.47 \text{ } \mu\text{m}$ $h = 15.49\text{e-}3 \text{ mm}$ $V = 37.65\text{e-}4 \text{ mm}^3$ $k = 10.5\text{e-}5 \text{ mm}^3/\text{N.m}$	$d_1 = 836.12 \text{ } \mu\text{m}$ $d_2 = 934.07 \text{ } \mu\text{m}$ $h = 19.62\text{e-}3 \text{ mm}$ $V = 60.39\text{e-}4 \text{ mm}^3$ $k = 12.0\text{e-}5 \text{ mm}^3/\text{N.m}$
Top part	$d_1 = 689.74 \text{ } \mu\text{m}$ $d_2 = 806.72 \text{ } \mu\text{m}$ $h = 14.02\text{e-}3 \text{ mm}$ $V = 30.85\text{e-}4 \text{ mm}^3$ $k = 14.3\text{e-}5 \text{ mm}^3/\text{N.m}$	$d_1 = 792.46 \text{ } \mu\text{m}$ $d_2 = 823.65 \text{ } \mu\text{m}$ $h = 16.35\text{e-}3 \text{ mm}$ $V = 41.95\text{e-}4 \text{ mm}^3$ $k = 11.7\text{e-}5 \text{ mm}^3/\text{N.m}$	$d_1 = 828.58 \text{ } \mu\text{m}$ $d_2 = 933.75 \text{ } \mu\text{m}$ $h = 19.45\text{e-}3 \text{ mm}$ $V = 59.35\text{e-}4 \text{ mm}^3$ $k = 11.8\text{e-}5 \text{ mm}^3/\text{N.m}$

Table 16 - Zirconium sphere wear scars diameters, depth (h) and volume (V) of the wear scars, and wear rate (k) of the component P2.

	$F_N = 3 \text{ N}$	$F_N = 5 \text{ N}$	$F_N = 7 \text{ N}$
Bottom part	$d_1 = 542.50 \mu\text{m}$ $d_2 = 371.25 \mu\text{m}$ $h = 5.22\text{e-}3 \text{ mm}$ $V = 4.28\text{e-}4 \text{ mm}^3$ $k = 2.00\text{e-}5 \text{ mm}^3/\text{N.m}$	$d_1 = 575.55 \mu\text{m}$ $d_2 = 399.44 \mu\text{m}$ $h = 5.95\text{e-}3 \text{ mm}$ $V = 5.55\text{e-}4 \text{ mm}^3$ $k = 1.50\text{e-}5 \text{ mm}^3/\text{N.m}$	$d_1 = 828.32 \mu\text{m}$ $d_2 = 689.46 \mu\text{m}$ $h = 14.42\text{e-}3 \text{ mm}$ $V = 32.63\text{e-}4 \text{ mm}^3$ $k = 6.50\text{e-}5 \text{ mm}^3/\text{N.m}$
Top part	$d_1 = 639.63 \mu\text{m}$ $d_2 = 330.75 \mu\text{m}$ $h = 5.89\text{e-}3 \text{ mm}$ $V = 5.45\text{e-}4 \text{ mm}^3$ $k = 2.50\text{e-}5 \text{ mm}^3/\text{N.m}$	$d_1 = 517.15 \mu\text{m}$ $d_2 = 538.87 \mu\text{m}$ $h = 6.98\text{e-}3 \text{ mm}$ $V = 7.64\text{e-}4 \text{ mm}^3$ $k = 2.10\text{e-}5 \text{ mm}^3/\text{N.m}$	$d_1 = 821.09 \mu\text{m}$ $d_2 = 559.35 \mu\text{m}$ $h = 11.93\text{e-}3 \text{ mm}$ $V = 22.33\text{e-}4 \text{ mm}^3$ $k = 4.40\text{e-}5 \text{ mm}^3/\text{N.m}$

Comparing the wear rates on the sphere, between the powder and the wire component, it is possible to understand that the wire component presents the higher values of wear rate.

It is also possible to identify a difference between the top and base portions, as it was expected given the microhardness variations throughout the vertical axis of the component.

The overall tendency, was to register higher values of wear rate on the top portion of the components, which is presumably linked with the higher microhardness that is characteristic of this portion of the components, that ultimately increases the wear suffered by the zirconium sphere.

However, looking only at the results of the tests that used 7 N of normal force, this tendency shifts, with the higher wear rates being registered on the base portion. This variation could be related to the fact that, under the highest normal load, the pressure is high enough to deform the metallic material closing the porosity, therefore reducing the porosity influence on the wear.

On component W2, a significant variation between the base and top portions of the specimen was registered especially for the lower values of the normal force, with the top portion registering a wear rate that almost doubles the one registered on the base portion of the component.

Following the wear data analysis, the next point of interest, is the geometry of the wear track on the stationary plane side.

The following graphs (Figs. 50-51) present the wear track cross section geometry for both the W2 and P2 components, for the base and top part of each component, with the three applied normal force values (3, 5 and 7 N).

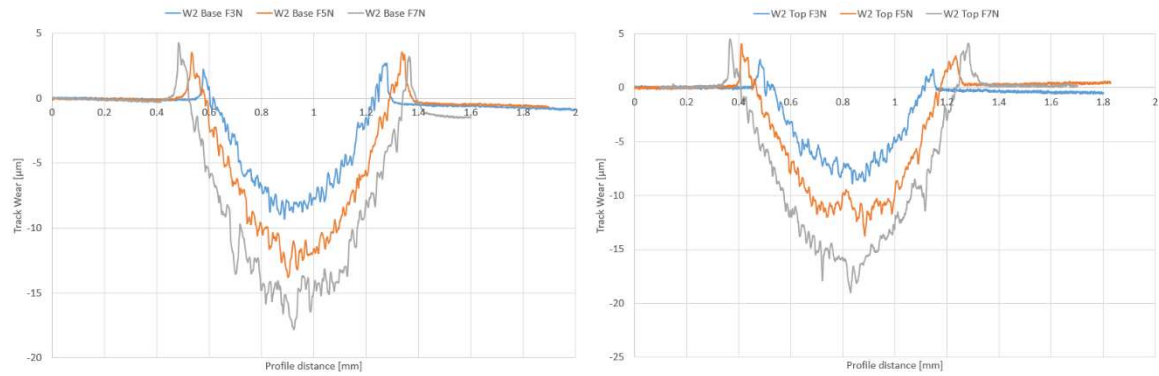


Figure 50 - Cross section profiles from the wear tracks on the base part (left) and top part (right) of the W2 component, for 3, 5 and 7 N of normal force.

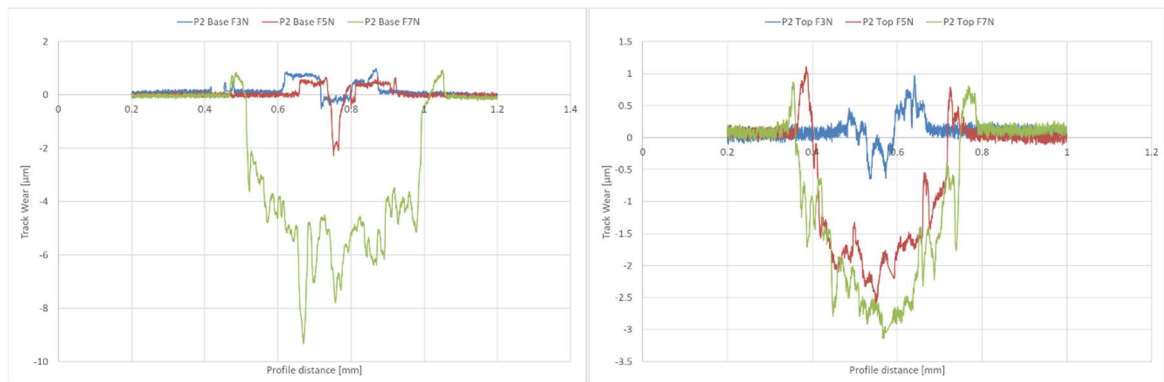


Figure 51 - Cross section profiles from the wear tracks on the base part (left) and top part (right) of the P2 component, for 3, 5 and 7 N of normal force.

In order to calculate the cross section area and then the total volume, and therefore achieve a similar analysis to the one that was applied to the zirconium sphere wear scars, the data had to be worked, and some approximations had to be made.

All the wear profiles cross sections were approximated to quadratic curves, so that these could then be integrated to achieve the area.

The cross sections were divided into three separate quadratic curves, represented in figure 52, as $y_1(x)$, $y_2(x)$ and $y_3(x)$, which assume an equation of the type $ax^2 + bx + c = y(x)$, with a, b and c, being constants that can be calculated recurring to the coordinates of three points from each individual quadratic curve, them being the start, the end and the maximum/minimum.

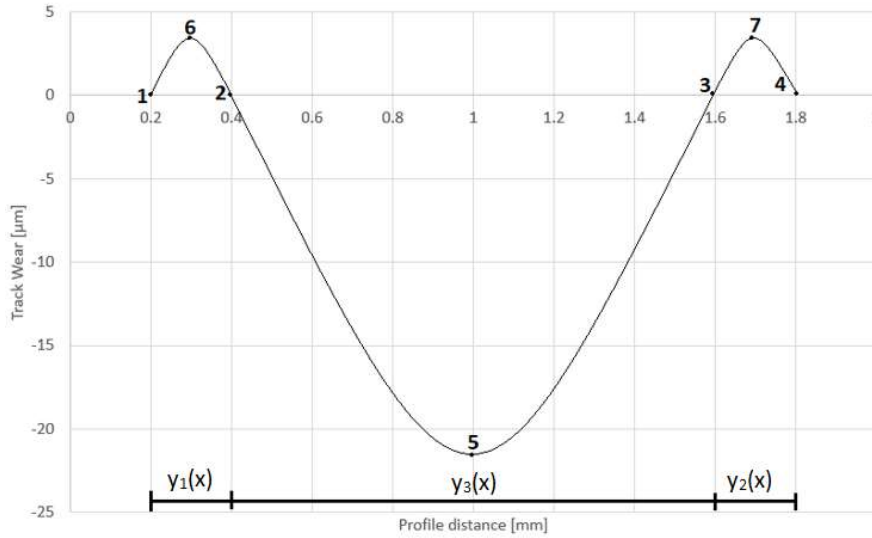


Figure 52 - Quadratic curves used to represent the wear profiles cross sections.

Using the coordinates of points 1 to 7, and the resulting equations of the three quadratic curves, the area of the cross section can then be calculated through the integration of those curves.

Tables 17 to 20 present the coordinates of points 1 through 7 for both the W2 and P2 components, on the base and top portions.

Table 17 - Point coordinates of the quadratic curves used to represent the wear profile cross section on the W2 specimen base part.

	3 N		5 N		7 N	
	x	y	x	y	x	y
Base						
1	0.5440	-0.1187	0.4780	-0.0117	0.4390	-0.1653
2	0.6040	-0.0774	0.5920	-0.2119	0.5270	-0.3455
3	1.2470	0.0649	1.2920	0.1594	1.3360	-0.8394
4	1.3270	-0.4057	1.3930	-0.1925	1.4450	-1.2413
5	0.8880	-9.1388	0.9020	-13.8027	0.9260	-17.7466
6	0.5800	2.1499	0.5340	3.4421	0.4850	4.1017
7	1.2730	2.6687	1.3360	3.4449	1.3650	3.0935

Table 18 - Point coordinates of the quadratic curves used to represent the wear profile cross section on the W2 specimen top part.

	3 N		5 N		7 N	
	x	y	x	y	x	y
Top						
1	0.4430	0.0317	0.3780	0.0594	0.3290	0.19
2	0.5380	-0.0923	0.4690	-0.0512	0.4090	0.1385
3	1.1130	-0.2629	1.1800	0.3212	1.2390	0.2754
4	1.1610	-0.0469	1.2640	0.3695	1.3380	0.2983
5	0.8360	-8.8253	0.8840	-13.5422	0.8290	-18.924
6	0.4820	2.6024	0.4140	3.7785	0.3700	4.3366
7	1.1140	1.6387	1.2350	2.8859	1.2810	4.0916

Table 19 - Point coordinates of the quadratic curves used to represent the wear profile cross section on the P2 specimen base part.

Base	3 N		5 N		7 N	
	x	y	x	y	x	y
1	0,6058	0.0783	0.6560	-0.0324	0.4675	-0.0489
2	0.7175	-0.0028	0.7400	-0.0364	0.5125	-0.1345
3	0.7995	-0.0162	0.8115	0.0583	0.9940	-0.6951
4	0.8825	0.1320	0.9310	0.0653	1.0640	-0.0426
5	0.7190	-0.5257	0.7525	-2.2728	0.7575	-7.7945
6	0.6805	0.8013	0.6925	0.5510	0.4905	0.7391
7	0.8675	0.9590	0.8730	0.6231	1.0505	0.9241

Table 20 - Point coordinates of the quadratic curves used to represent the wear profile cross section on the P2 specimen top part.

Top	3 N		5 N		7 N	
	x	y	x	y	x	y
1	0.4825	0.0113	0.3655	0.0887	0.3405	0.1161
2	0.5280	-0.0022	0.4015	-0.0607	0.3605	0.0553
3	0.5925	0.1427	0.7190	0.0621	0.7495	-0.0038
4	0.6685	0.1299	0.7650	0.0468	0.7905	0.0489
5	0.5735	-0.6338	0.5505	-2.6256	0.5690	-3.1392
6	0.4870	0.4585	0.3865	1.0542	0.3550	0.8147
7	0.6410	0.9686	0.7270	0.7440	0.7720	0.7430

The results of the integration, that directly represent the cross section area of the wear profile, are presented below (tables 21 and 22), as well as the wear track volume, which is the result of the multiplication of the wear track area by the wear track length, which was of 2mm.

Table 21 - Wear profile cross section approximate area of specimen W2 base and top parts.

	Base part		Top part	
	Total area [mm ²]	Volume [mm ³]	Total area [mm ²]	Volume [mm ³]
3 N	0.004212	0.008424	0.003643	0.007286
5 N	0.007014	0.014028	0.00478	0.009560
7 N	0.010169	0.020338	0.013512	0.027024

Table 22 - Wear profile cross section approximate area of specimen P2 base and top parts.

	Base part		Top part	
	Total area [mm ²]	Volume [mm ³]	Total area [mm ²]	Volume [mm ³]
3 N	0.001172	0.002344	0.000121	0.000242
5 N	0.000262	0.000524	0.000638	0.001276
7 N	0.002661	0.005322	0.000852	0.001704

Before analysing the wear track cross-section area, it is important to calculate the wear rate on the component side. To do so, equation (5) is used, and the results are presented below, in table 23 and figure 53, for both the powder and wire components.

Table 23 - Wear rate coefficient on the plane side, for both the W2 and P2 components.

	W2			P2		
Normal force	3 N	5 N	7 N	3 N	5 N	7 N
Base wear rate coefficient [mm ³ /Nm]	14.03e-7	14.03e-7	14.53e-7	3.91e-7	0.52e-7	7.8e-7
Top wear rate coefficient [mm ³ /Nm]	12.14e-7	9.56e-7	19.3e-7	0.4e-7	1.28e-7	1.22e-7

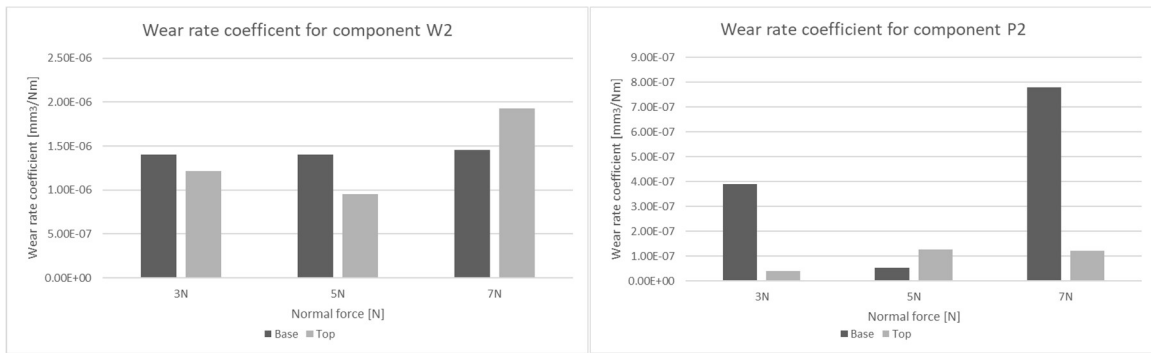


Figure 53 - Comparison between the base and top wear rate coefficients, for component W2 (left) and component P2 (right).

The following graph presents the variation of the wear profile cross section area differences between the top and base parts of the components W2 and P2.

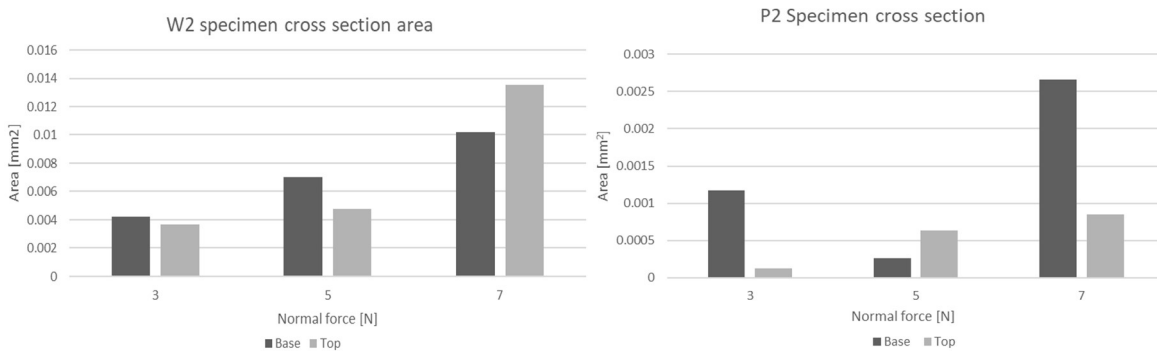


Figure 54 - Comparison between the base and top cross section area of the wear profile, on W2 (left) and P2 (right) specimens.

Even though there is a difference in magnitude between the wear rate coefficient and the cross-section area of the wear tracks, for both the components being tested, it is possible to observe that the tendencies that register regarding the wear rate coefficients are the same that register regarding the cross-section area of the wear tracks.

With regard to the analysis of the profile of the wear track resulting on the flat specimen it can be verified that there is also a clear relationship between the transverse area of the cavity and the normal force on specimen surface during the test.

It is possible to verify that with the increase of normal force there is also an increase in both the profile depth and the profile width for both the W2 and P2 components (Figure 54).

The results of the upper and lower portion of the component present a similar tendency and range, with higher values of area of the cavity achieved for a normal force exerted in the specimen of 7 N.

However, the differences observed in the behaviour of both the top and base parts of the components, do not allow any specific conclusions.

For component W2 lower values of normal force (3 and 5 N) translate in bigger wear profile cross section area on the base part of the component, where microhardness is lower, however, when using higher normal force (7 N), the same cross section area is much bigger on the top part than on the lower part, which was not expected since the higher microhardness was registered on the top part, but the mass transferred due to wear during sliding could have an influence on this issue.

Following this principle, this could be linked to the fact that the removed material could increase the wear and help to create a wider and deeper wear track, given that the material that is being removed directly from the cavity has a presumably higher hardness than the material of the component itself, thus causing much higher wear rate, ending up in a larger area being removed by the end of the test. This effect is only observed on the higher value of normal force tested. That could be justified by the fact that when using lower values of normal force the top components with higher microhardness prevent the wear of material, because the amount of removed material is not enough to play a role on the wear process.

For component P2, that same exact tendency is observed, but the critical normal force is registered at 5 N, where the cross-section area is larger for top portion rather than the bottom portion.

When applying a normal force of 3 N, the cross-section area of the wear track on the top portion is very small, indicating very little wear, or that some compounds could be formed with the materials that are removed from the zirconium sphere and from the component itself, that deposit inside the cavity, artificially lowering the value of cross-section area.

As for the 5 N of normal force test, the top portion registers a bigger cross-section area, with a possible justification being the one presented for the 7N of normal force test on component W2, with the removed material hardness being higher than the one on the component, thus helping the wear process, ending in a bigger wear track.

For the 7 N of normal force, a new tendency is observed, with a much higher cross-section area being registered on the base part of the component. The same justification could apply with the removed material being harder than the component, helping the wear process. As

for the top portion, the cross-section area is much smaller than the one registered on the base portion, meaning that the removed material could be depositing into the cavity, and closing the porosity, thus creating difficulty to the wear process, or, again, artificially increasing the cross section area of the wear track.

5. Conclusion

On the introductory chapter a few facts were presented, with the majority of them pointing towards a scenario where the parameters that are used to produce a component through the LMD technology have an influence that is yet relatively unknown and undocumented.

The main goal of this work was to study the mechanical properties of several LMD components produced with both powder and wire LMD processes, using several deposition heights on the powder LMD components, in order to understand how they would compare between themselves, and how their mechanical properties would compare to the references.

The microhardness data collected allowed the understanding that on each component, the values of microhardness vary significantly from one point to another, with the top of the components, where the last layers were deposited, tending to present a higher microhardness when compared to the one registered on the base, for all of the tested components. The overall values of microhardness were significantly higher than the reference ones, for both the powder and the wire components.

This all points towards a scenario where the cooling process and the time in which it develops has a high influence on the microhardness of the components.

This tendency carried to the friction and wear data, where it was observed that the microhardness had a contribution to the friction and wear that occurred in the tested components.

Regarding the friction data, the coefficient was higher for the powder LMD component, however, in both cases, it was clear that normal force applied does not influence the friction coefficient significantly.

However, in some cases, the microhardness had an influence, with a different behaviour being observed, like it was the case with sample P2 to loads 5 and 7 N, where it was necessary to wait 100 seconds before the start of the increasing of friction coefficient, meaning that the material that is being removed from the component was probably forming some sort of compounds together with the material that was being removed from the zirconium sphere, which in the end could be facilitating the sliding process, thus keeping the friction coefficient

in a non-steady state. In other cases, the steady-state regime was observed faster, which was the expected behaviour prior to the tests.

The wear rate on the used zirconium sphere was higher with contact on wire LMD components, pointing that the lower microhardness that this component presented translated into a higher wear. However, the normal force and the wear rate were not proportional, indicating that the material that is being removed from the component could be having an active role on the wear process.

As for the cross-section area of the wear tracks, and the wear rate coefficient, it was possible to observe that the tendency was higher values of area and wear rate, for higher values of normal force applied, although in some points this tendency did not verify.

As for the base and the top of the components, some differences were registered between them, with the tendency being higher areas and wear rates on the base of the components. Despite this tendency, some specific values of normal force generated a higher area and wear rate on the top rather than on the base, with a possible explanation being that the removed material, which has a higher microhardness than the one on the component, helping the wear process.

Another important aspect was the strong indication that the components had a relatively high porosity since electro-discharge machining failed to perform a cut on the components, and the density test somewhat confirmed this suspicion. However, the small dimensions of the density test specimens made the confirmation of a high porosity somewhat inconclusive.

However, this suspicion of high porosity, ended up being somewhat confirmed, when an additional density measurement was conducted, during the impulse excitation of vibration test, with the results pointing towards density values, below the reference ones.

A well-arranged microstructure was observed, as well as a good layer arrangement, with the powder component presenting some visible gaps that could explain the suspicious of high porosity on the powder components.

As for the mechanical properties evaluated with the impulse excitation of vibration test, it is possible to conclude that the powder component presented properties much comparable to the reference values of the material with which it was manufactured. As for the wire component, the registered properties were lower than the reference.

With all of the collected data and information it was possible to understand the mechanical properties of the components that are produced through powder and wire LMD.

However, it is not safe to say that these components could present themselves as a strong alternative to the automotive industry and to the processes that are commonly used in it.

A high variability of mechanical properties and also a poor surface finish was observed on the manufactured components. That suggests the LMD and process control is still under a significant development, in order to achieve a good reproducibility, factor that is key when considering a process for an industry that is so time and resource demanding as the automotive industries.

6. Future work

Regarding future works, it is possible to identify a few tasks, that would help to not only clarify some of the conclusions that were drawn from this project, but also to add to it, with new information.

Firstly, one of the important tasks, would be to conduct macrohardness tests on the components, in order to clarify if the standard deviation variation is associated with any sort of error. This test would also help to understand the macrohardness of the components, which should not be subjected to as much variation as the microhardness was.

Secondly, it would be interesting to conduct all of the mentioned mechanical tests, with components produced with conventional manufacturing techniques using both the Metco 42C (similar to AISI 431 stainless steel) and the AISI 316L stainless steel, used to manufacture both the powder and the wire LMD components, respectively. This would help to clarify the comparison between LMD and conventional techniques.

Additionally, it would also be interesting, to conduct the friction and wear tests, using the available LMD components, with conditions that could emulate a scenario where an LMD produced component was used as a part of a combustion engine. The used metallic materials are often present in engine parts, such as intake and exhaust manifolds, shafts, among other parts, which are subjected to conditions where some chemical substances are present. The friction and wear test allow to add to the conditions that the specimens are subjected chemical substances, which could emulate the use in an engine. This would help clarify, if the chemical substances have an influence on the wear suffered by the components.

Bibliography

- [1] – "Additive Manufacturing - ASTM International", *Astm.org*, 2019. [Online]. Available: <https://www.astm.org/industry/additive-manufacturing-overview.html>. [Accessed: 20- Mar- 2019].
- [2] – Anton, K., "Production of hard metal alloys" U.S. Patent 2,076,952A, issued 1934.
- [3] – O.J. Munz, "Phot-glyph recording" U.S. Patent 2,775,758, issued 1956.
- [4] – W.K. Swainson, "Method, medium and apparatus for producing three-dimensional figure product" U.S. patent 4,041,476, issued 1977.
- [5] – A. Ciraud, "Process and Device for the Manufacture of any Objects Desired from any Meltable Material", *FRG Disclosure Publication 2263777*, 1972.
- [6] – R.F. Housholder, "Molding process" U.S. patent 4,247,508, issued 1981.
- [7] – H. Kodama, "Automatic method for fabricating a three-dimensional plastic model with photo-hardening polymer", *Review Scientific Instruments 52, 1770*, 1981.
- [8] – Y. Zhai, D. Lados and J. LaGoy, "Additive Manufacturing: Making Imagination the Major Limitation", *JOM*, vol. 66, no. 5, 2014.
- [9] – B. Selective Laser Sintering, "Selective Laser Sintering, Birth of an Industry - Department of Mechanical Engineering", *Me.utexas.edu*, 2019. [Online]. Available: <http://www.me.utexas.edu/news/news/selective-laser-sintering-birth-of-an-industry#ch4>. [Accessed: 27- Sep- 2019].
- [10] – W.E. Frazier, "Metal additive manufacturing: a review", *Journal of Materials Engineering and Performance*, vol.23, no.6, pp.1917-1928, 2014.
- [11] – D. Sher, "The global additive manufacturing market 2018 is worth \$9.3 billion", *3D Printing Media Network*, 2019. [Online]. Available: <https://www.3dprintingmedia.network/the-global-additive-manufacturing-market-2018-is-worth-9-3-billion/>. [Accessed: 27- Sep- 2019].

- [12] – M. Gnam, R. Plourde, and T. McDonald, “Laser Engineered Net Shaping (LENS),” Paper Presented at the National Center for Manufacturing Sciences, JTEG Business Meeting, 2000.
- [13] – S.M. Kelly, “Cost Benefit Analysis of Direct Digital Manufacturing” in *Private Communications*, ARL Penn State University, 2010.
- [14] – S. Phinazee, “Efficiencies: Saving Time and Money with Electron Beam Free Form Fabrication”, *Fabricator*, pp. 15–20, 2007.
- [15] – M.E. Kinsella, “Additive Manufacturing of Superalloys for Aerospace Applications”, WPAFB AFRL, Report Number AFRL-RX-WP-TP2008-4318, Dayton OH 2008.
- [16] – Gary K. Lewis, E. S., “Practical considerations and capabilities for laser assisted direct metal deposition”, *Materials and Design*, 21, pp. 417-423, 2000.
- [17] – A. Azarniya et al., "Additive manufacturing of Ti–6Al–4V parts through laser metal deposition (LMD): Process, microstructure, and mechanical properties", *Journal of Alloys and Compounds*, vol. 804, pp. 163-191, 2019.
- [18] – B. Graf, S. Ammer, A. Gumenyuk and M. Rethmeier, "Design of Experiments for Laser Metal Deposition in Maintenance, Repair and Overhaul Applications", *Procedia CIRP*, vol. 11, pp. 245-248, 2013.
- [19] – S. Oliari, A. D'Oliveira and M. Schulz, "Additive Manufacturing of H11 with Wire-Based Laser Metal Deposition", *Soldagem & Inspeção*, vol. 22, no. 4, pp. 466-479, 2017.
- [20] – "| Directory French SME Aerospace | Aerospace | France | SME Aerospace", *Espace-aeronautique.com*, 2019. [Online]. Available: <https://www.espace-aeronautique.com/cgi-bin/fiche.asp?lang=ANG&code=BeAM1052>. [Accessed: 27- Sep- 2019].
- [21] – *Lortek.es*, 2019. [Online]. Available: http://www.lortek.es/files/merlin/03-P_Hagqvist-UW&GKN-Aero-Case-study.pdf. [Accessed: 27- Sep- 2019].
- [22] – S. Kaierle, A. Barroi, C. Noelke, J. Hermsdorf, L. Overmeyer and H. Haferkamp, "Review on Laser Deposition Welding: From Micro to Macro", *Physics Procedia*, vol. 39, pp. 336-345, 2012.

- [23] – R. Vilar, "Laser Alloying and Laser Cladding", *Materials Science Forum*, vol. 301, pp. 229-252, 1999.
- [24] – U. Midtgard and J. Jernes, "Toxicology and occupational hazards of new materials and processes in metal surface treatment, powder metallurgy, technical ceramics, and fiber-reinforced plastics.", *Scandinavian Journal of Work, Environment & Health*, vol. 17, no. 6, pp. 369-379, 1991.
- [25] – Markusson L., "Powder characterization for additive manufacturing process". Lulea University of Technology, Sweden, 2017.
- [26] – C. Mogueira, Trumpf Portugal, 2018.
- [27] – "Bharat Industries -Blog - Wire Drawing", *Wiredrawingdies.co.in*, 2019. [Online]. Available: <http://www.wiredrawingdies.co.in/wire-drawing/>. [Accessed: 27- Sep- 2019].
- [28] – R. Poprawe, *Tailored Light 2*. Berlin, Heidelberg: Springer Berlin Heidelberg, 2011.
- [29] – "Cutting Reflective Metals with a Laser | SPI Lasers", *SPI Lasers*, 2019. [Online]. Available: <https://www.spilasers.com/application-cutting/cutting-reflective-metals-with-a-laser/>. [Accessed: 27- Sep- 2019].
- [30] – "Process", *Additec.net*, 2019. [Online]. Available: <https://www.additec.net/process/>. [Accessed: 27- Sep- 2019].
- [31] – "Wirefeed Additive Manufacturing vs. Powder Methods | Sciaky", *Sciaky.com*, 2019. [Online]. Available: <https://www.sciaky.com/additive-manufacturing/wire-vs-powder>. [Accessed: 27- Sep- 2019].
- [32] – I. Microtrac, "Manufacturing Metal Powder", *AZoNano.com*, 2019. [Online]. Available: <https://www.azonano.com/article.aspx?ArticleID=4683>. [Accessed: 27- Sep- 2019].
- [33] – *Assets.lia.org*, 2019. [Online]. Available: <https://assets.lia.org/s3fs-public/pdf/conferences/%233%20-%20Wire%20vs%20Powder%20in%20LMD.pdf>. [Accessed: 27- Sep- 2019].
- [34] – *Interlloy.com.au*, 2019. [Online]. Available: <http://www.interlloy.com.au/our-products/stainless-steel/431-martensitic-stainless-steel-bar/>. [Accessed: 27- Sep- 2019].

- [35] – D. Paschotta, "Lasers", *Rp-photonics.com*, 2019. [Online]. Available: <https://www.rp-photonics.com/lasers.html>. [Accessed: 27- Sep- 2019].
- [36] – M. Alves, "Tecnologias Laser", Leiria, 2018.
- [37] – I. Garmendia, "LMD Components", 2018.
- [38] – "C45 / DIN 1.0503 Carbon steel | AISI 1045 | S45C-Fuhong steel", *Fuhongforge.com*, 2019. [Online]. Available: <http://www.fuhongforge.com/din-1-1191-c45e-carbon-steel/>. [Accessed: 27- Sep- 2019].
- [39] – I. Garmendia, J. Leunda, J. Pujana and A. Lamikiz, "In-process height control during laser metal deposition based on structured light 3D scanning", *Procedia CIRP*, vol. 68, pp. 375-380, 2018.
- [40] – Oerlikon.com, 2019. [Online]. Available: https://www.oerlikon.com/ecomaXL/files/metco/oerlikon_DSMTS-0080.7_Martensitic_SS_Powder.pdf&download=1. [Accessed: 27- Sep- 2019].
- [41] – *Steeleaglemalta.com*, 2019. [Online]. Available: <https://www.steeleaglemalta.com/?wpdmact=process&did=NjkuaG90bGluaw==>. [Accessed: 27- Sep- 2019].
- [42] – *Metals handbook*. Metals Park, Ohio: American Society for Metals, 1988.
- [43] – *Csun.edu*, 2019. [Online]. Available: <http://www.csun.edu/~bavarian/Courses/MSE%20528/MicroHardnessLab.pdf>. [Accessed: 27- Sep- 2019].
- [44] – A. 17, "ASTM E92 - 17 Standard Test Methods for Vickers Hardness and Knoop Hardness of Metallic Materials", *Astm.org*, 2019. [Online]. Available: <https://www.astm.org/Standards/E92.htm>. [Accessed: 27- Sep- 2019].
- [45] – A. 11(2017), "ASTM E3 - 11(2017) Standard Guide for Preparation of Metallographic Specimens", *Astm.org*, 2019. [Online]. Available: <https://www.astm.org/Standards/E3.htm>. [Accessed: 27- Sep- 2019].

- [46] – "ETCHING", *Metkon.com*, 2019. [Online]. Available: <http://www.metkon.com/mobile/Applications-Details/63/ETCHING/>. [Accessed: 27- Sep- 2019].
- [47] – "Metallographic Etchants", *Metallographic.com*, 2019. [Online]. Available: <https://www.metallographic.com/Etchants/Etchants.htm>. [Accessed: 27- Sep- 2019].
- [48] – A. E1876-01, "ASTM E1876 - 01 Standard Test Method for Dynamic Youngs Modulus, Shear Modulus, and Poissons Ratio by Impulse Excitation of Vibration", *Astm.org*, 2019. [Online]. Available: <https://www.astm.org/DATABASE.CART/HISTORICAL/E1876-01.htm>. [Accessed: 27- Sep- 2019].
- [49] – "Friction and Friction Coefficients for various Materials", *Engineeringtoolbox.com*, 2019. [Online]. Available: https://www.engineeringtoolbox.com/friction-coefficients-d_778.html. [Accessed: 27- Sep- 2019].
- [50] – *Rgpballs.com*, 2019. [Online]. Available: <https://www.rgpballs.com/srv/sheet.ashx?pid=66&lng=en>. [Accessed: 27- Sep- 2019].
- [51] – A. Ramalho, M. Braga de Carvalho and P. Antunes, "Effects of temperature on mechanical and tribological properties of dental restorative composite materials", *Tribology International*, vol. 63, pp. 186-195, 2013.
- [52] – "Properties: Stainless Steel - Grade 431 (UNS S43100)", *AZoM.com*, 2019. [Online]. Available: <https://www.azom.com/properties.aspx?ArticleID=1023>. [Accessed: 27- Sep- 2019].